SMAST Technical Report 12-0301

Transient Tidal Eddy Motion in the Western Gulf of Maine

W. S. Brown and G. M. Marques

School for Maine Science & Technology
University of Massachusetts Dartmouth
New Bedford, MA

Abstract

In early April 2005, a pair of high-frequency Coastal Ocean Dynamics Applications Radar (CODAR) stations on Cape Cod and Nantucket MA mapped clockwise (CW) and anticlockwise (ACW) eddy motion shortly after maximum ebb and flood tidal current, respectively. These observations were validated by M_2 tide-forced, high-resolution, QUODDY finite-element numerical ocean model simulations of the formation of eddy motion near the coast offshore of Chatham, MA in our Great South Channel (GSC) study domain of the western Gulf of Maine. To better elucidate the kinematics and dynamics of these eddy motions, observational and model investigations were conducted during the very weakly stratified winter 2008-09 conditions. The 5-constituent tidally-forced QUODDY model hindcast simulations mapped the formation, evolution and across-GSC translation of ebb flow-forced CW and flood flow-forced ACW eddy motions after the respective maximum flows. The field measurements consisted of moored bottom pressure and ADCP current measurements at a nearshore site (TTE) in 13m depth. Tidal hindcast current series were generated using the 5 principal tidal constituents at several historical sites in water depths of ~33m within 30km of the TTE site. The currents in this observational study region were dominated by M_2 semidiurnal currents which trace highly-rectified ~60km peak-to-peak elliptical paths in the along-shore direction along (~ 30^o-210^oT). The observation- and the model-based eddy motion kinematics are consistent with CW or ACW eddy motions that (a) grow near shore in the coastal boundary layer (CSL) for about 4hrs after the respective ebb or flood current maxima and (b) then translate southeastward along curved 50m isobath at speeds of about 25 m/s across the GSC. The observation-based momentum budget estimates in the inner 15km (Inner Zone average depth ~20m) were dominated by a balance between the alongshore pressure gradient and quadratic bottom friction forces; with a much weaker inertial force. In the deeper (Outer Zone average depth ~30m) offshore 15km, all three terms contributed more evenly to the momentum budget. Relative to observations, model runs using a bottom drag coefficient Cd = 0.005 produced currents which were too large by about 50%, while runs with Cd = 0.010 were in better agreement with observation-based results that used Cd=0.010-friction. Based on Cd=0.010-based bottom friction estimates, we found that the Inner Zone observation-based estimates of rate change of vorticity was balanced primarily by the vorticity diffusion terms. We conclude that transient eddy motions in the GSC region (1) is generated by a combination of strong alongshore pressure gradients and the bottom friction gradients in the shallower nearshore; (2) are phase eddies that are part of the change of tide across the GSC; (3) require a better understanding of the bottom friction environment in their shallow water origin . Finally the model results strongly suggest that the hydrodynamic nonlinearities induce asymmetry in the alternating eddy motions, which could induce significant biases the regional secondary upwelling/downing environment.

Introduction

Tide-induced eddy motions are found in many different coastal ocean regions featuring curved coastlines and promontories (Pingree, 1978; Pingree and Maddock, 1980; Wolanski et al., 1996; Geyer and Signell, 1990). Many of these studies report on the secondary flows associated with tide-induced eddy motions. For example, Geyer (1993), using tidal current data offshore of Gay Head, Martha's Vineyard, reports that secondary flow represents about 20% of the principal tide-induced eddy motions. However, there are indications that the dynamics of these eddy motions and their associated secondary flows differ.

Surface current maps of the region east of Cape Cod, MA from early April 2005 (Brown and Yu, 2006) suggest the formation of alternating clockwise (CW) and anticlockwise (ACW) eddy motions in association with respective ebb and flood tidal flows (see Figure 1). Both of these eddy features translate southeastward into the central Great South Channel (GSC) region of the western Gulf of Maine (GoM); and then disappear near the end of the ebb (or flood) flow phase. These eddy motions have been detected in high frequency (HF =5 MHz) radar-derived surface current maps of the region east of Cape Cod, MA. Mid Atlantic Regional Association Coastal Ocean Observing System (MARACOOS)-supported Coastal Ocean Dynamics Applications Radar (CODAR) installations near Nauset, MA and on Nantucket Island (see Figure 1) provide hourly surface current maps that routinely extend about 100km offshore from Chatham, MA (at the elbow of Cape Cod) covering the Great South Channel of the western Gulf of Maine.

These HF-radar derived current observations are supported by realistic numerical tidal model simulations, which also clearly reveal the transient upwelling and down welling secondary flows that are associated with both the primary and eddy motions. The persistent presence eddy motions and their associated downwelling and upwelling can be potentially important environmental factors for applications ranging from search and rescue forecasting to recruitment to the regional fisheries. More specifically, the details of this secondary flow environment may be important to the settlement of scallop larvae (i.e., spat) and/or the general maintenance of the local scallop fishery (Stokesbury et al., 2004).

To address questions regarding basic transient tidal eddy motion characteristics and mechanisms, we conducted a field observation/model study during the winter of 2008-09 when the stratification was very weak. In this paper, we describe the kinematics and dynamics of the primary tide-induced eddy motion circulation in the Great South Channel in the western Gulf of Maine. In a companion paper (Marques and Brown, 2011 – henceforth MB11) the focus is on the induced secondary flows and their modulation by the primary eddy motion.

This paper is organized as follows. The field measurements and basic observational results are presented in section 1. The numerical modeling including the model setup and the basic model surface current maps are presented in section 2. In section 3, there is first a comparison between observational and modeling results. In section 4, we present a

synthesis of the observations and model results concerning the kinematics of the formation and evolution of the tidal eddy motion. In section 5, we focus on the momentum and vorticity dynamics concerning the formation of the tidal eddy motion. The discussion of results and summary of conclusions appears in section 6.

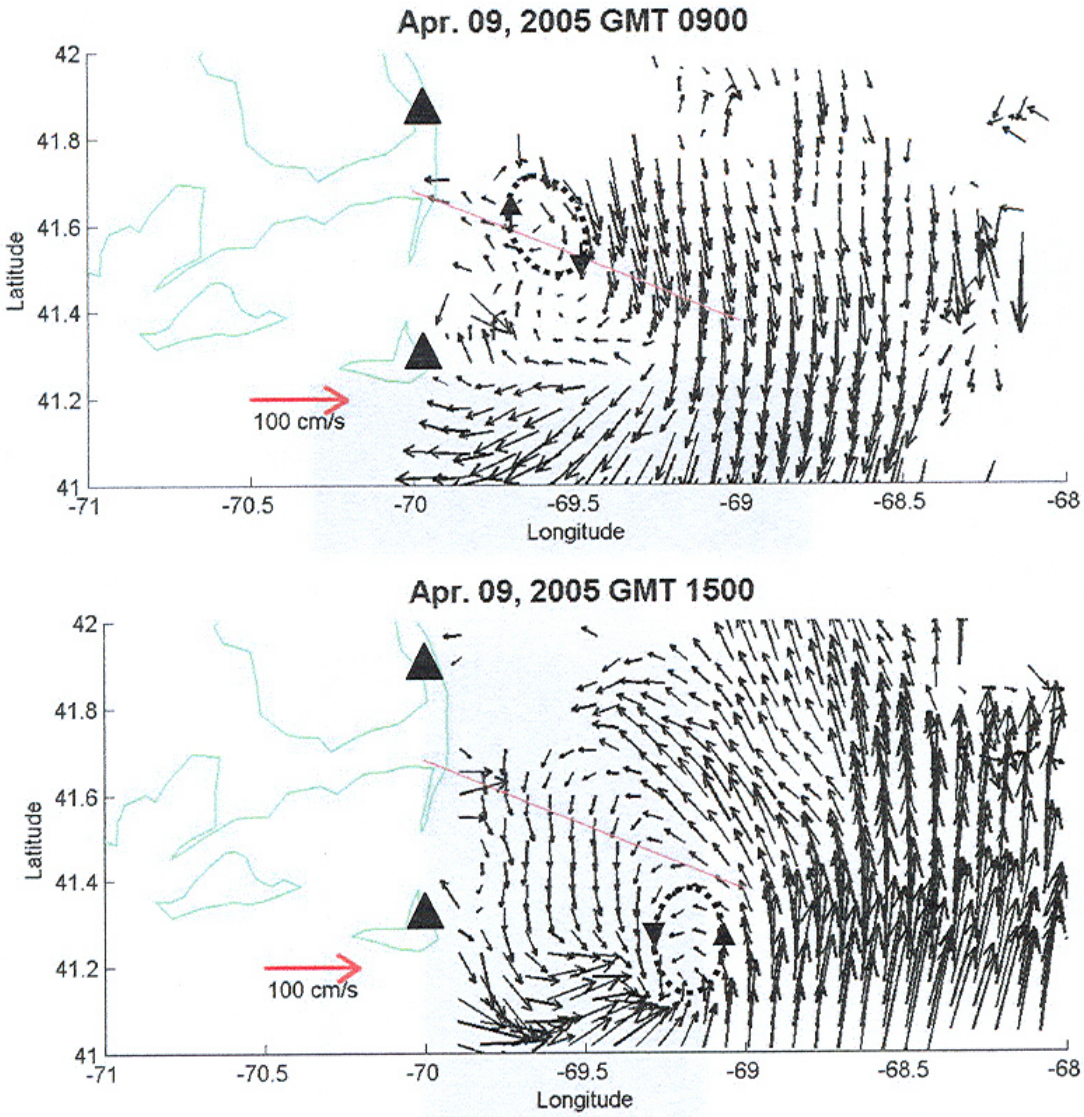

Figure 1 The hourly surface current map that was derived from measurements of radial currents by high-frequency radar (CODAR) sites at Nauset and Nantucket (triangles) at 0900 and 1500 UTC 9 April 2005. (above) Clockwise and (below) anticlockwise transient tidal eddy motion east of the elbow of Cape Cod and northeast of Nantucket is suggested by the current patterns (after Brown and Yu, 2006).

1. Basic Observational Results

The field component of the study was conducted between 3 November 2008 and 27 January 2009. A bottom-mounted instrument with an Acoustic Doppler Current Profiler (ADCP) and pressure sensor was deployed at station TTE (Figure 2; Table 1) on

3 November 2008 and recovered on 27 January 2009. A shipboard CTD water property survey was conducted along the across-isobath transect (Figure 2) on 27 January 2009.

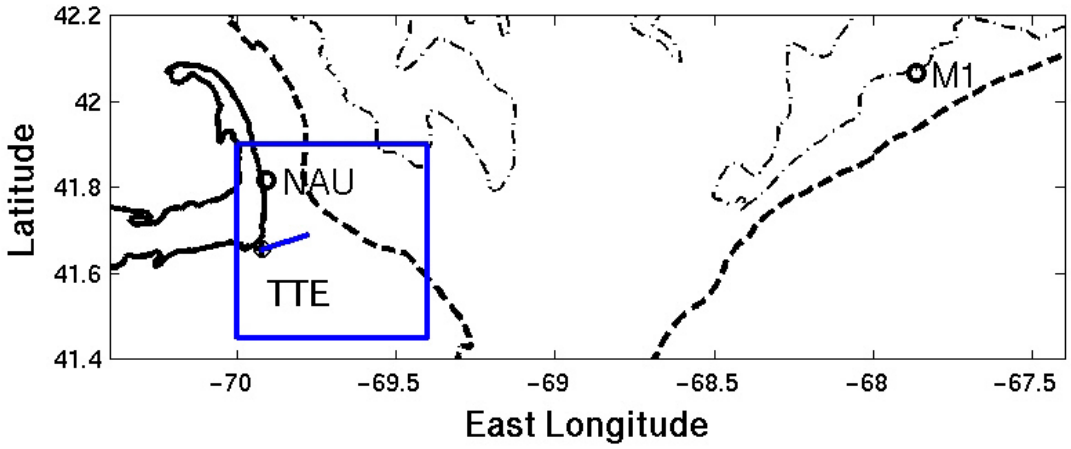

Figure 2 Location map of the study region (box) in the Great South Channel region. The TTE moored current/bottom pressure station (cross-circle) and hydrographic survey transect are located; as are the auxiliary bottom pressure stations at Nauset (NAU) and on the north flank of Georges Bank (M1). The 100m and 200m isobaths are shown.

Table 1 Station TTE bottom pressure and current record information, including station depths, measurement depths, and measurement record lengths, is given; along with that for the tidal harmonic constants from historical measurement stations/given by Moody et al. (1984).

Station ID	**Station Longitude** ^{o}W	**Station Latitude** ^{o}N	**Station Depth** (m)	**Record Depth** (m)	**Record Length** (days)
PRESSURE					
TTE	69. 923	41.658	13	12	58
Nauset	69.933	41.817	7	6	58
M1	67.867	42.067	184	179	556
CURRENT					
TTE	69. 923	41.658	13	6, 8	58
NSA	69.600	41.520	33	5, 25	60
NSB	69.730	41.430	23	10	42
NSD	69.730	41.620	33	16	42

A. The Measurements

Shipboard Hydrography: A recently-calibrated, internally-recording Seabird® SBE-25 Sea-logger was used to measure conductivity (C) and temperature (T) versus pressure (P) profiles during a 7-station cross-shelf survey on 27 January 2009 (details in Brown et al., 2009a). The hydrographic water property sections in Figure 3 show a relatively well-mixed water column (< 0.26 sigma-t units) in the study region inside of the 50m isobaths. The weak salinity-induced density stratification was very similar to that reported upon by Shcherbina and Gawarkiewicz (2008), who measured hydrography a few kilometers north of our study site during a recent winter.

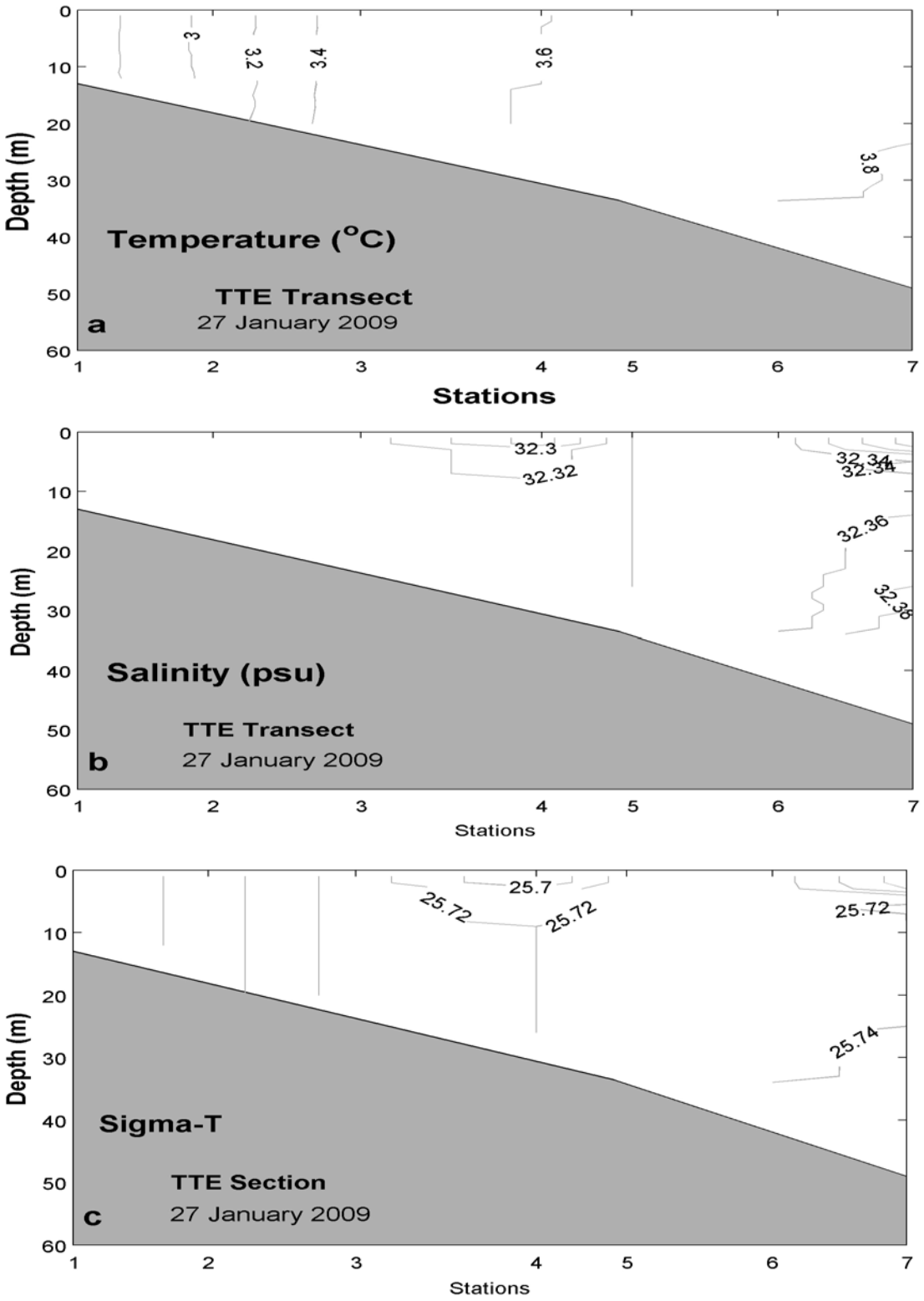

Figure 3 The 27 January 2009 vertical sections of **(a)** temperature (CI = 0.10°C), **(b)** salinity **(**CI = 0.05 psu) and **(c)** density anomaly (sigma-t; CI = 0.02)) at the indicated stations 1 through 7 (left to right).

Moored Measurements: A bottom instrument package, with an upward-looking RDI 300 kHz Workhorse ADCP and Aanderaa TR-7 pressure sensor (for details see Brown et al. 2009b), was deployed at station TTE (41^o 39.5'N - 69^o 55.4'W; see Table 1) off of Chatham, MA on 3 November 2008; and recovered on 27 January 2009. A 2 ½ month record of 5-minute bottom pressure (BP) samples (see Figure 4) had an uncertainty of ± 0.10dbar (consistent with a least count resolution of ~0.33dbar - see Figure 5). The 2-month records of 10-minute average ADCP northward and eastward current samples at 6m and 8m above-bottom (AB) (see Figure 5) were composed of 10-minute average samples with an estimated uncertainty of ± 0.05m/s.

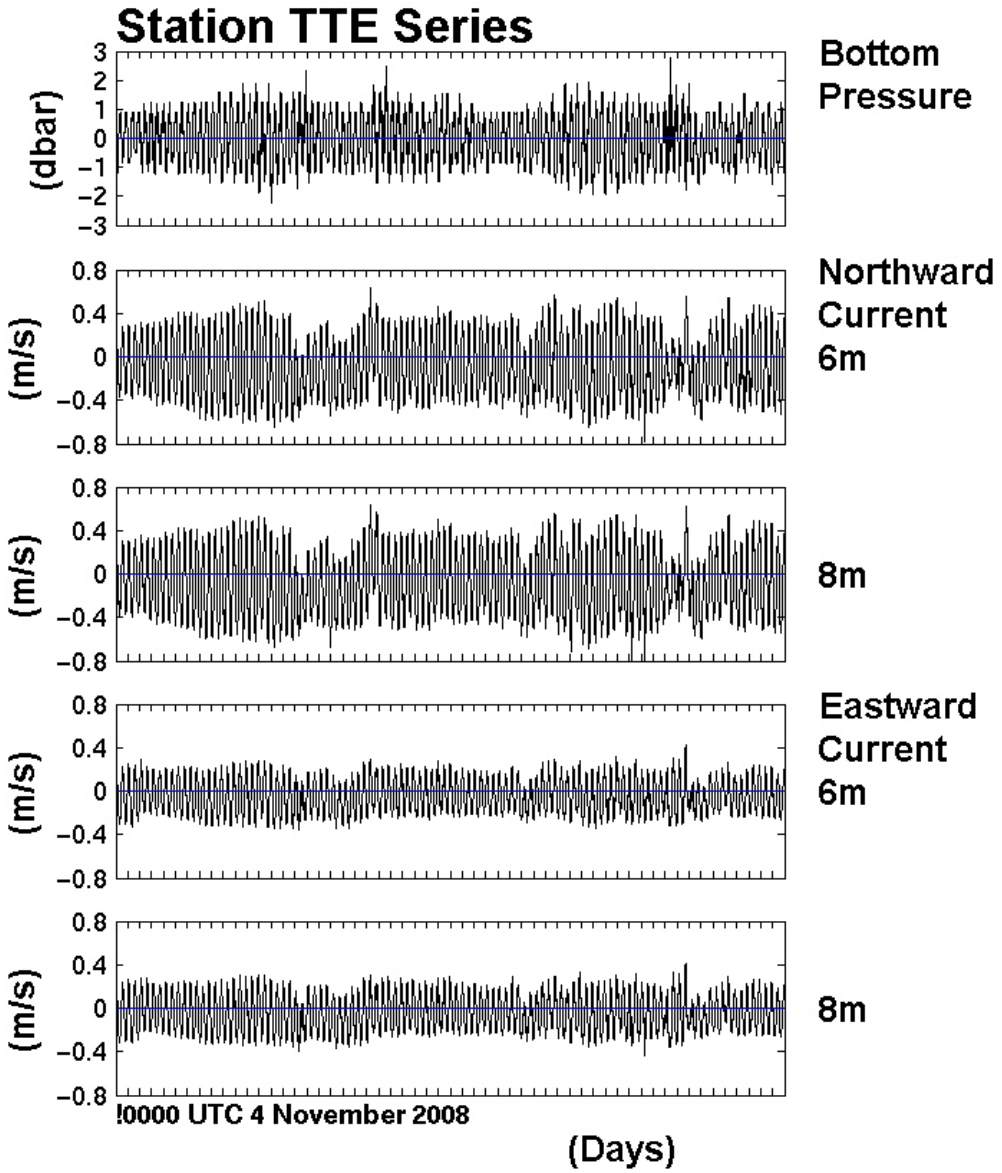

Figure 4 Station TTE time series measurements records; (**upper**) bottom pressure; **(2 middle)** ADCP northward currents at 6m and 8m AB and **(2 bottom**) eastward currents.

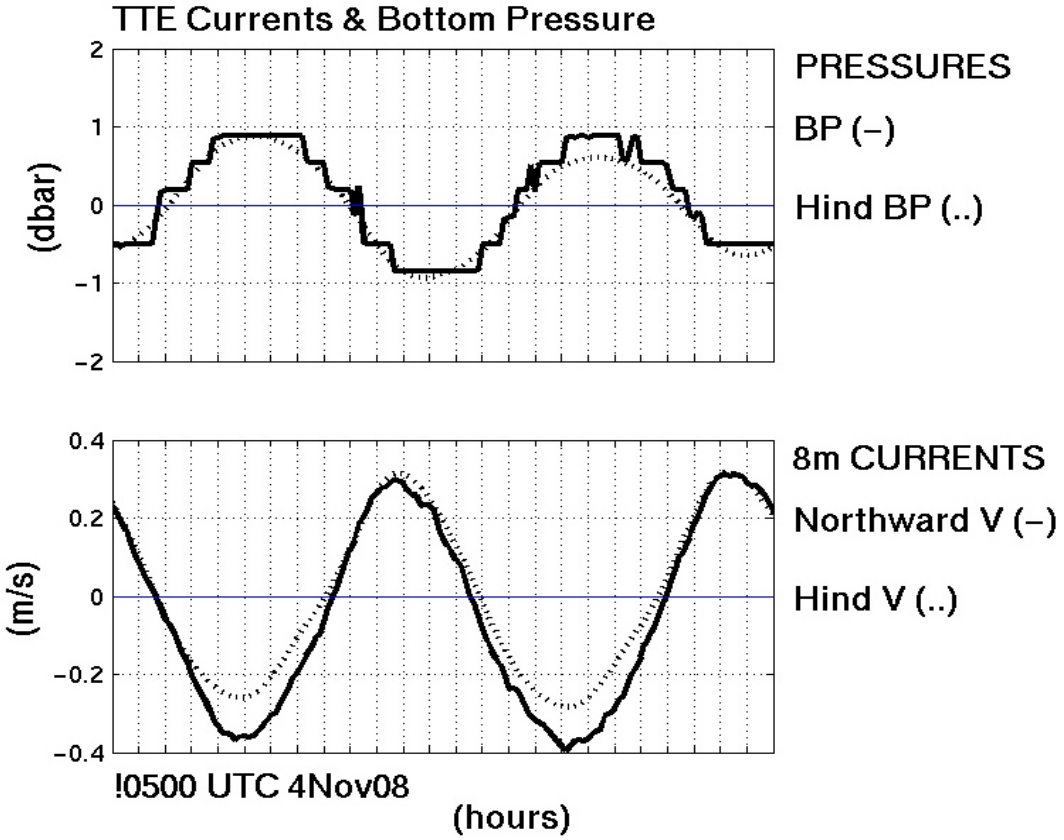

Figure 5 A 25-hr zoom of the station TTE moored measurements and their tidal hindcast counterparts (dotted). **(upper)** Bottom pressure displaying the measurement least count resolution and **(lower)** 8m AB northward ADCP-measured current.

The similarity in the station TTE 6m and 8m current fluctuations is not surprising given the dominating semidiurnal tidal currents in 13m depth. A comparison between shipboard and moored ADCP current measurements on 4 November 2008 verified the accuracy of the ADCP measurements. A series mean flow, which is 9.2 cm/s (see Table 2) towards 206^{o}T, is superposed on a fluctuating current, with an ellipse with rms amplitude of 0.34 m/s and orientation along 19^{o}-199^{o}T. About 50% of the mean current can be attributed rectified tidal current flow as determined by our model computations (see below).

The results of a harmonic analysis of the current time series at station TTE show that fluctuating currents at 6m and 8m are dominated by nearly identical M_2 tidal currents, with near-rectilinear motions oriented along 30^{o}T - 210^{o}T (see Figure 6; Table 3; Appendix A). (Note: These tidal currents are aligned with bathymetric grooves in the vicinity of the mooring). The set of hindcast tidal records that were produced for the full 85-day study period (Figure 7) illustrate the spring-neap tidal cycles during the study period. The measured r*esidual* series were produced by removing the hindcast tidal records from the full series (also in Figure 7). The residual series energy was about 1/10 of that of the full series; emphasizing the dominance of the tidal response of the region. These measurements of the tidal variability of the TTE study region were complemented with the application of an ocean

circulation model as described next.

Table 2 Basic statistics of the moored ADCP currents in 2m bins bracketing depths of 8m and 6m above the bottom (AB) in an average of 13 m at station TTE. The current ellipses are given in terms of major axis amplitude, direction and ellipticity (ε = major/minor). The statistics are also given for the non-tidal residual (RES) currents as well as the TTE bottom pressure records.

Station TTE	**Mean** (cm/s)	**SD** (cm/s)	**Var** $(cm/s)^2$	**Total Var** $(cm/s)^2$	**rms Major Axis Amp** (cm/s)	**Major Axis Dir** (^oT)	**ε**
CURRENTS							
8m AB TOTAL				1249	35.1	19	8.1
Northward	-8.5	30.9	954				
Eastward	-4.1	17.2	295				
RES				140	11.2	13	2.9
Northward	-8.5	10.5	110				
Eastward	-4.1	5.4	30				
6m AB TOTAL				1118	33.2	19	8.9
Northward	-8.0	29.3	859				
Eastward	-4.1	16.1	259				
RES				116	10.3	14	3.1
Northward	-8.0	9.6	91				
Eastward	-4.2	5.0	25				
BOT PRESSURE		(dbar)		(dbr^2)			
1m AB TOTAL		0.851		0.724			
RES		0.265		0.070			

Table 3 The harmonic constants for the 5 principal + nonlinear tidal constituents of the station TTE eastward and northward current components 8m AB are based on an analysis of the 56 day records between 3 November and 29 December 2008. The current component amplitudes and Greenwich epoch phases are given along with the ellipses in terms of major axis amplitude/orientation and ellipticity (ε=major/minor; positive values mean anticlockwise-rotating current vector), and maximum current phase.

Tidal Const.	**East Amp** (cm/s)	**Phase** (G^o)	**North Amp** (cm/s)	**Phase** (G^o)	**Major Axis Amp** (cm/s)	**Major Dir** (^oT)	**ε**	**Phase** (G^o)
M_2	**23.0 ±0.5**	**272 ± 1**	**40.7 ±1.1**	**275 ± 1**	**46.7**	**30**	**42**	**274**
N_2	3.9 ±0.5	244 ± 7	7.0 ±1.1	252 ± 9	8.0	29	16	251
S_2	2.1 ±0.5	312 ±12	6.7 ±1.1	312 ± 7	7.0	17	∞	313
K_1	0.9 ±0.5	296 ±35	1.7 ±1.1	260 ±39	1.9	25	-4	268
O_1	0.2 ±0.4	335 ±75	0.1 ±0.1	129±106	0.2	282	∞	334
M_4	1.0	139	2.2	116	2.3	21	4	170
M_6	0.9	18	0.6	296	1.1	56	11	21

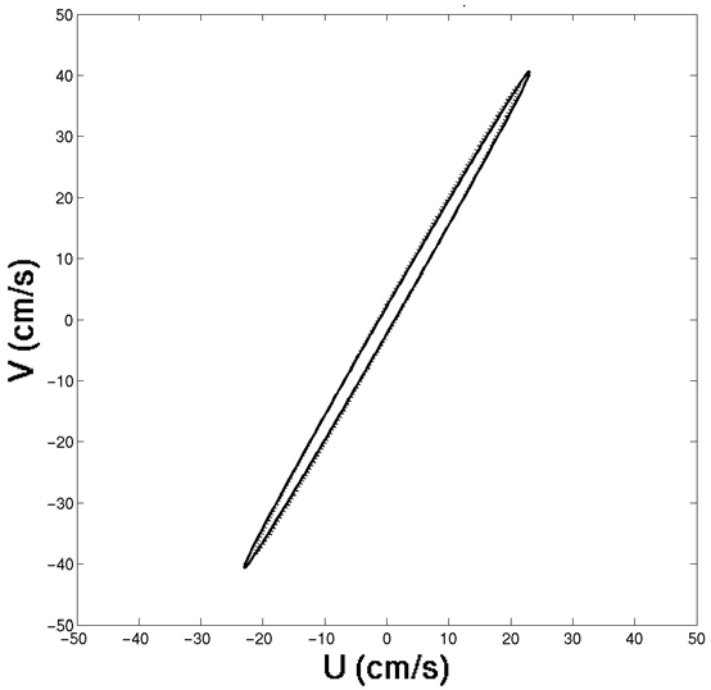

Figure 6 The station TTE 8m AB M_2 tidal current hodograph ellipse overlays an almost identical 6m AB ellipse.

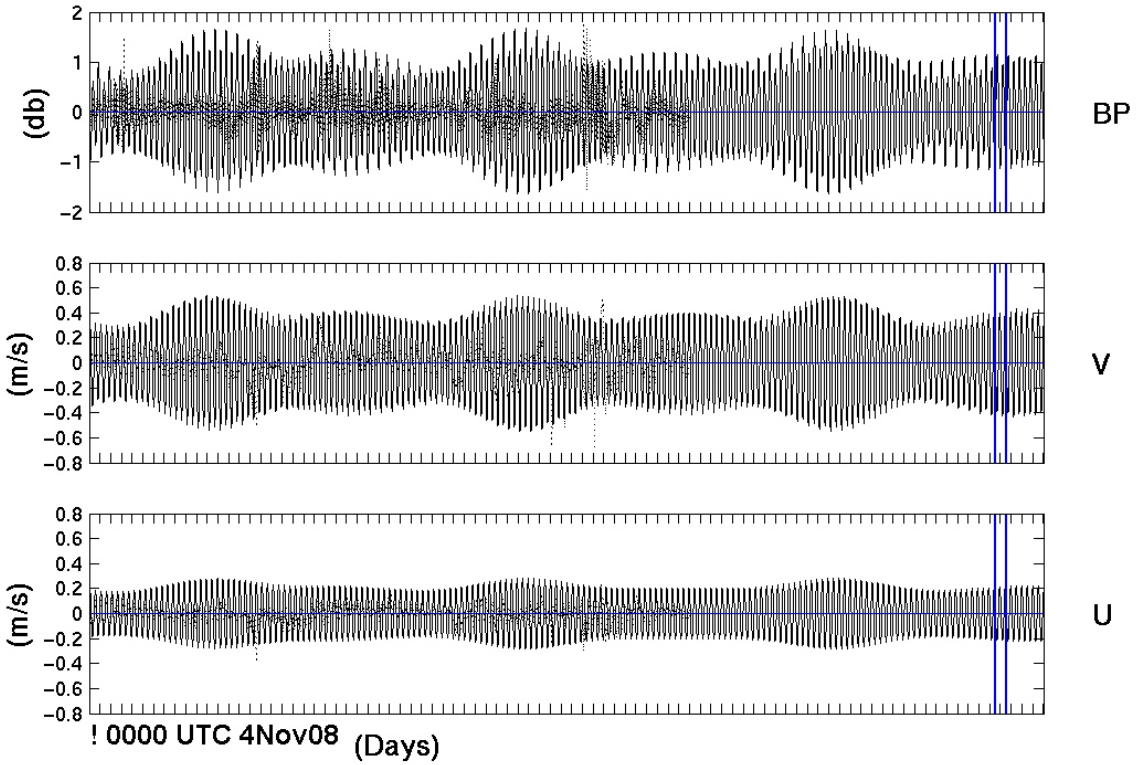

Figure 7 The station TTE *hindcast* tidal bottom pressure (BP), northward (V) and eastward (U) current at 8mAB for the full study period (4 November 2008 through 1 February 2009). The measured nontidal r*esidual series* (dotted) are superposed through December. The vertical lines bracket the 27-28 January 2009 time of analysis focus.

B. Eddy Motion Kinematics: Observations

The signatures of the transient tidal eddy motion of interest are found in a set of tidal hindcast time series of observed currents and bottom pressures (BP) from our TTE 13m depth station measurements; augmented by the Moody et al. (1984) historic BP stations off of Nauset, MA (NAU) and Georges Bank (M1) (see Figure 2) as well as current stations at NSA (33m), NSD (33m), and NSB (23m) respectively. Tidal BP and current time series were hindcast using the available suites of tidal harmonics for the five principal tidal constituents (M_2, N_2, S_2, O_1, and K_1). The major axes of the dominant M_2 current tidal ellipses in Figure 8 (see Table 4) reveal a general north northeastward orientation in the study region. (The more complete list of harmonic constants is in Appendix A). The phase differences in the maximum M_2 tidal current reflect the presence of tidal eddy motions as explained below.

Table 4 The M_2 constituent harmonic constants for the (a) *rotated* depth-averaged currents at stations TTE and NSA; (b) NSB 10m and NSD 16m currents; (c) *Inner Zone* currents – an average of TTE and P (see main text); and (d) *Outer Zone* currents from NSD and NSA. The current component amplitudes and Greenwich epoch phases are given along with the M_2 tidal current ellipse in terms of major axis amplitude and orientation, ellipticity (ε=major/minor for which a positive value indicates an anticlockwise rotating current vector), and the Greenwich epoch phase of the maximum current.

Tidal Cons	**Sta Dep** (m)	**U Amp** (cm/s)	**U Ph** (°G)	**V Amp** (cm/s)	**V Ph** (°G)	**Major Amp** (cm/s)	**Major Dir** (°T)	**ε**	**Max Ph** (°G)
OBS									
TTE	13	1.3	181	47.1	275	47.1	30	36	275
P	30	3.6	165	51.4	345	51.5	26	517	345
NSD	33	6.4	226	45.9	341	46.0	27	8	341
NSA	33	26.0	139	51.5	333	57.4	4	- 10	330
NSB	23	19	91	71	354	71	28	- 4	353
Inner Zone	*23*	*3*	*162*	*40*	*312*	*40*	*27*	*33*	*312*
Outer Zone	*32*	*14*	*153*	*49*	*337*	*51*	*14*	*-51*	*337*

The array of M_2 tidal current ellipses in Figure 8 were computed for the depth-averaged currents. (An inspection of model current profiles indicated that the mid-depth currents at stations NSD and NSB represented the local depth-averaged currents well). The general northeast-southwest orientation of the dominant M_2 tidal current ellipse major axes prompted us to rotate the analysis coordinate system 30° clockwise (see Figure 9) so as to more naturally align with these currents (i.e., X/U -> 120°T; Y/V ->30°T). The M_2 constituent harmonic constants for depth-averaged *rotated currents* at these stations are given in Table 4. Station TTE, NSD, and NSA were conveniently located for the anticipated analysis of tidal variability within an *Inner Zone* and an *Outer Zone*, while station NSB was significantly outside the study region. Thus tidal currents were estimated at station P (about 4 km south of station NSD in about 30m of water) by way of a space-weighted linear interpolation of hindcast currents at stations NSB and NSD (see Figure 9).

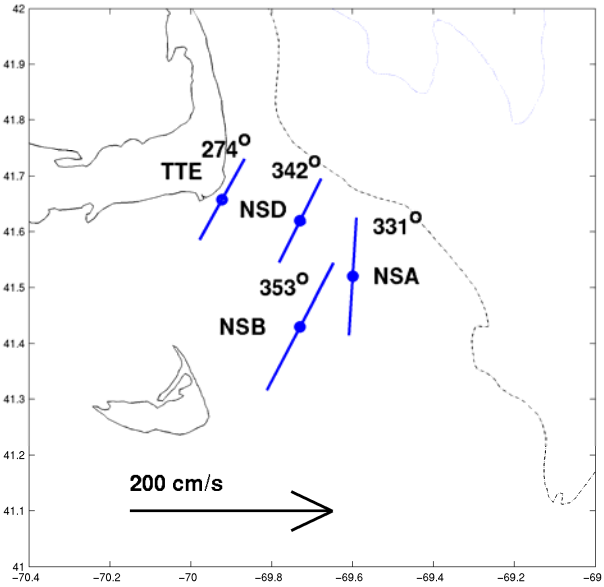

Figure 8 The M_2 tidal current ellipse axes for vertically-averaged measured currents at stations TTE, NSD, NSB, and NSA. The Greenwich epoch phases, for which lower values lead, indicate the maximum inflow currents. The 50m isobath is shown.

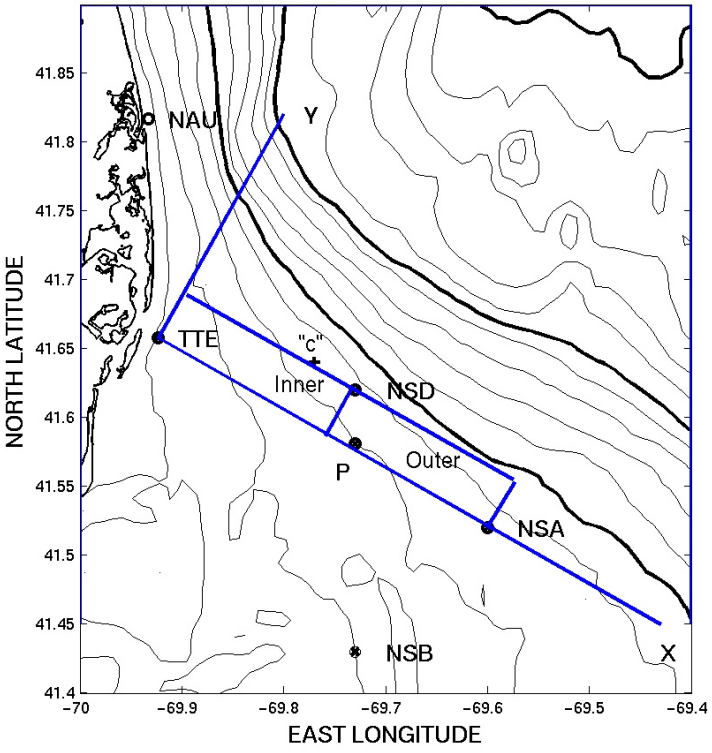

Figure 9 Location map of the current (x) and bottom pressure (o) stations. The tidal currents at station P were derived from a weighted-average of tidal hindcast tidal currents at NSB and NSD (see text). The normal Cartesian coordinate system was rotated clockwise 30° to align it more closely with the regional tidal flow (see Figure 10). The shallower (~25m) *Inner Zone* and deeper (-35m) *Outer Zones* are defined. The study region isobaths are given in 10m intervals to 100m; then 20m intervals into deeper waters. The 50m, 100m, and 200m isobaths are bolder. The site of the He and Wilkin (2006) model momentum budgets is marked by "c".

The M_2 tidal current ellipses at stations TTE, P, NSD, and NSD provide the first clues the nearshore eddy formation in the study region. The individual M_2 water parcel displacement ellipses indicate similar 50km to 60km northeast to southwest excursions (Figure 10). However, there are large phase differences in maximum currents across the 30km array; with TTE current leading others by 55^o–70^o (2.4 hours). These phase differences are the signatures of the alternating anticlockwise (ACW) and clockwise (CW) eddy motion that traverse the study as shown below.

Further, the M_2 tidal current vectors underlying these station elliptical patterns rotate ACW in the *Inner Zone* and CW in the *Outer Zone* (Table 4). This difference tidal ellipse characteristics indicate that our study region is located on the cusp of what Brown (1984) found to be a progressive Sverdrup M_2 tidal wave regime over Georges Bank and a near-standing wave regime within the GoM proper.

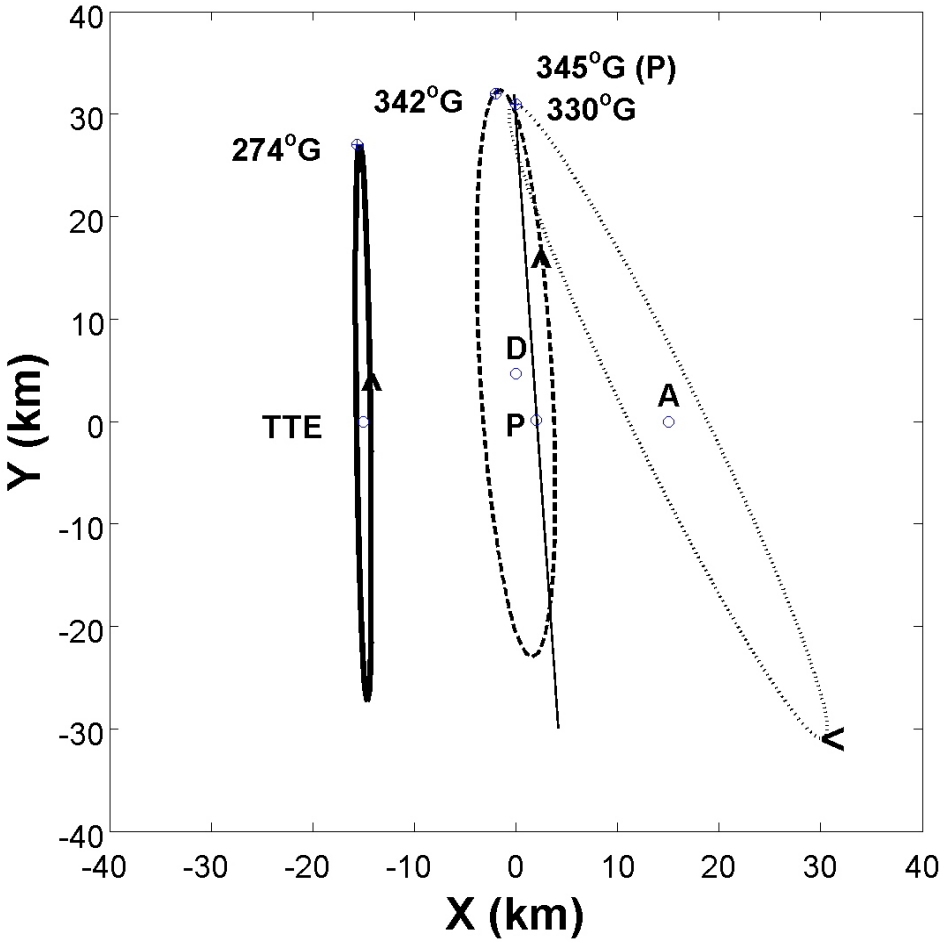

Figure 10 The M_2 tidal cycle progressive vector diagrams (PVD) for estimates of the depth-averaged currents at stations TTE (- bold), NSD (--), NSA (...) and P (- thin). The ellipses are located to scale according to the array geometry. The Greenwich phases of the maximum flood currents (lower phase values lead) are given along with the sense of the current vector rotation. Note the change from ACW motion at stations TTE, P, and D to CW motion at station D. Up is toward 30^oT.

2. Numerical Modeling

The Lynch et al. (1996, 1997) high-resolution finite-element coastal ocean circulation model QUODDY was employed to simulate the tide-dominated currents in the study region. The weak stratification during the study justified our use the barotropic mode of QUODDY. The model was forced with hindcast 5-constituent (M_2, N_2, S_2, O_1, and K_1) sea level along the open ocean boundaries of the model domain; as defined by the Holboke (1998) unstructured mesh called GHSD (see Figure 11). The model lateral resolution in this application varied from about 10 km in the Gulf of Maine (GoM) interior, to about 5 km near the coastlines, with even finer kilometer-scale resolution in the regions of steep bathymetric slopes (e.g., north flank of Georges Bank). The vertical structure was resolved with 21-sigma layers from the 10m minimum depth at the coastal boundary elements throughout the model domain. The model results considered here were produced every 1/16th M_2 tidal cycle for the time periods of simulation.

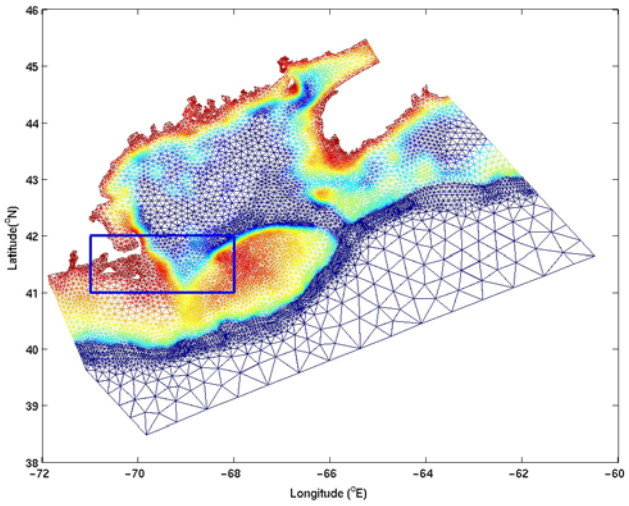

Figure 11 The greater Gulf of Maine region is partitioned with the finite-element mesh (GHSD, Holboke, 1998) that is used with the 3-D finite element coastal ocean model – QUODDY, with color-coded depths. The box delineates the extended study region, for which the zoom is presented in Figure 12.

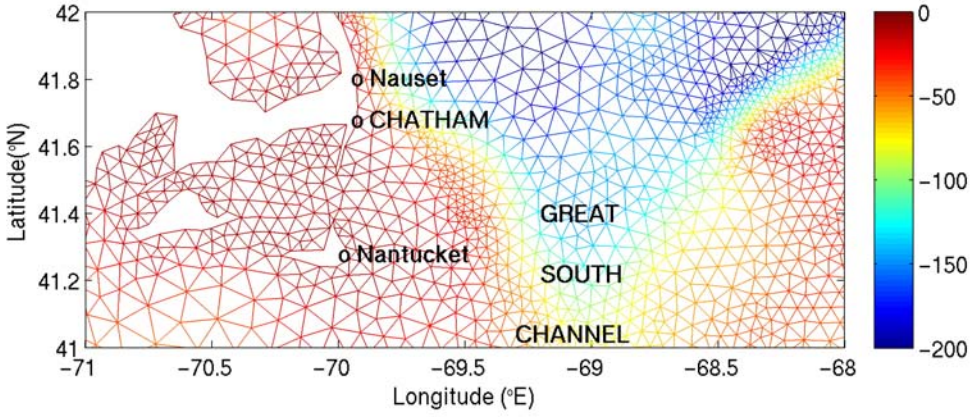

Figure 12 This zoom of the study region (defined in Figure 11) shows the model finite element resolution as well as color-coded water depths (meters).

A. The Model

QUODDY is a 3-D, nonlinear, prognostic, f-plane, finite-element coastal ocean circulation model with advanced turbulence closure (Lynch et al., 1996; 1997). In this application, bottom flow $\overrightarrow{V_b}$ is subject to quadratic bottom boundary stress, according to $C_d \mid V_b \mid V_b$, where the time/space constant bottom drag coefficient C_d is 0.005. There was no surface forcing imposed for this study.

The conditions imposed on the different QUODDY open ocean boundaries are for:

- *Deep Ocean and the Northeastern and Southwestern Cross-Shelf Sections*: Hindcast semidiurnal M_2, N_2, S_2 and diurnal K_1 and O_1 elevation series, based the Mukai et al. (2002) EastCoast 2001 tidal harmonics database that was derived from a harmonic analysis of simulations of ADvanced CIRCulation (ADCIRC) finite-element hydrodynamic numerical model.

- *Bay of Fundy Section:* Hindcast Normal flows for the M_2, M_4, M_6, N_2, S_2, K_1 and O_1 tidal constituents based on the harmonic constants derived from a simulation using the linear numerical model FUNDY6 – a predecessor of QUODDY with linear dynamics.

The barotropic QUODDY model calculation, which was initialized with zero velocity and elevation fields, was run with a 21.83 second (= the 12.42-hour M_2 tidal period/2048) time-step. To allow the model to reach dynamical equilibrium, the amplitude of the prescribed tidal forcing was linearly increased to full forcing (i.e., ramped-up) during the first six M_2 tidal cycles of the model run. Holboke (1998) has shown that the QUODDY advection and nonlinearities dynamically adjust to the initial fields with such a ramp-up.

Marques and Brown (2009) found that the quality of this QUODDY model application (with 5-tidal constituent forcing) was generally very good in terms of model minus observation differences of the harmonic constants at the Moody et al. (1984) 49-stations. The differences were particularly small for the M_2 tidal sea level amplitudes, with a percentage mean, mean ±standard deviation of differences between the observation-based and the mean and standard deviation of the M_2 tidal sea level amplitudes were 7.7%, 0.051 ±0.045 m; phases were 3.5 ±3.8°G, respectively. The corresponding percentage mean difference, mean ±standard deviation for N_2 were 13.6%, 0.026 ±0.022m; phases were 12.2 ±6.0°G; for S_2 were 18.0%, 0.030 ±0.019m; phases were 15.1 ±9.7°G; for K_1 were 28.0%, 0.022 ±0.017m; phases were 11.2 ±8.2°G; and for O_1 were 10.8%, 0.009 ±0.008m; phases were 8.9 ±9.5°G, respectively.

B. Eddy Motion Kinematics: Model Surface Currents

The details of the regional kinematics of the tidal eddy motion formation and evolution process are revealed in the hourly sequence of model surface current maps

in Figure 13. The first in the sequence at 1558 GMT 27 January 2009 (Figure 13a) shows strong model ebb currents along the east-facing coast of Cape Cod, with a diminishing flood flow further east in the Great South Channel (GSC).

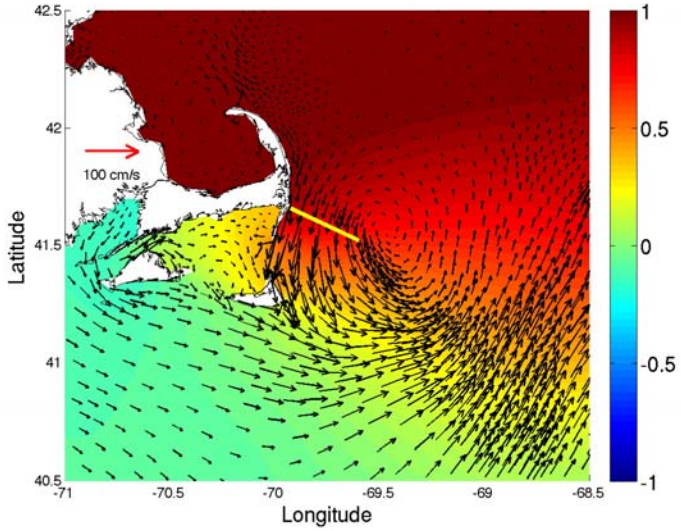

Figure 13a Model surface current and color-coded sea level (m) at **EBB$_{full}$-2hr** (1557[36] UTC 27 Jan)**.** The yellow bar spans stations TTE and NSA.

After 2 hours, the tidal flow spans the GSC (Figure 13b) in what we define as "full ebb tidal flow" (or EBB$_{full}$). The reference time for the half tidal cycle explored here is the 1800 UTC 27 January 2009.

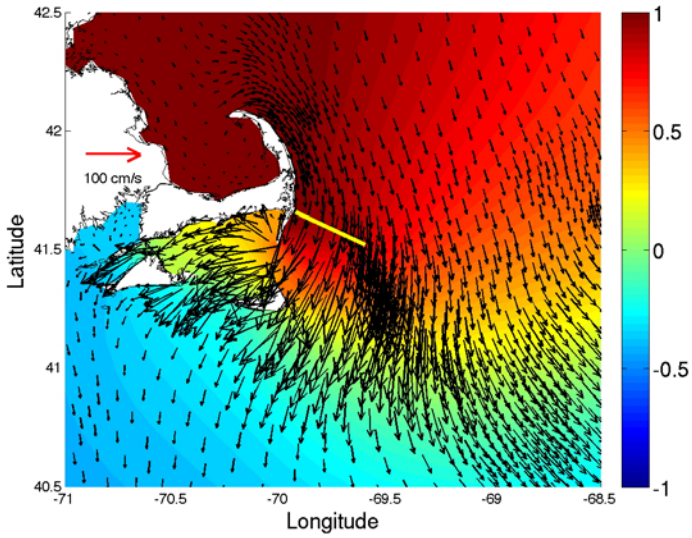

Figure 13b Model surface current and color-coded sea level (m) at **EBB$_{full}$+0hr (**1759[51] UTC 27 Jan)**.** The yellow bar spans stations TTE and NSA.

By EBB$_{full}$+1hr, the core of the main alongshore tidal flow in the Coastal Boundary Layer (or CBL, as defined by the *Inner Zone*) begins to bulge offshore (not shown).

By 2002 UTC (EBB_{full}+2hr), there is a distinct envelop shoreward of the alongshore flow in the separating CBL; suggesting the nearshore development of clockwise (CW) eddy motion (Figure $13c_{-1}$).

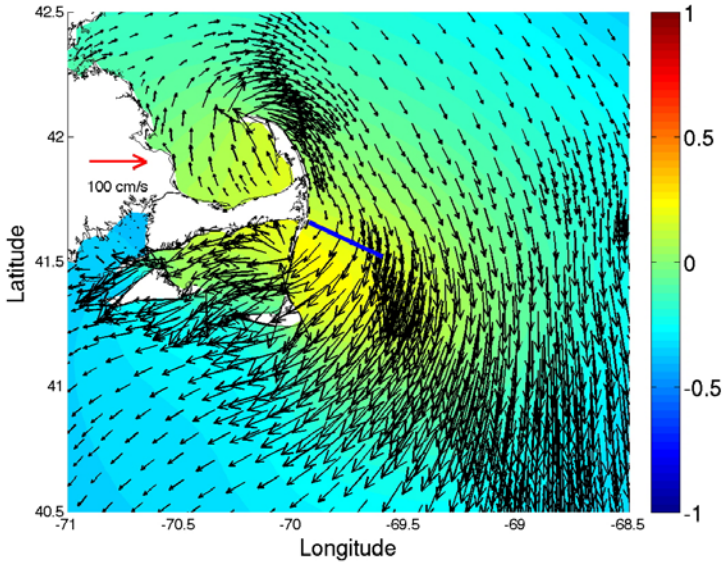

Figure $13c_{-1}$ Model surface current and color-coded sea level (m): **EBB_{full}+2.00hr** (2002[06] UTC 27 an)**.** The blue bar spans stations TTE and NSA.

A rapid bulging of the nearcoast alongshore flow, which is associated with the separating CBL, is seen in the Figure $13c_{-2}$ through Figure $13c_{-4}$ sequence. There is distinct tendency toward CW eddy motion within the flow envelop.

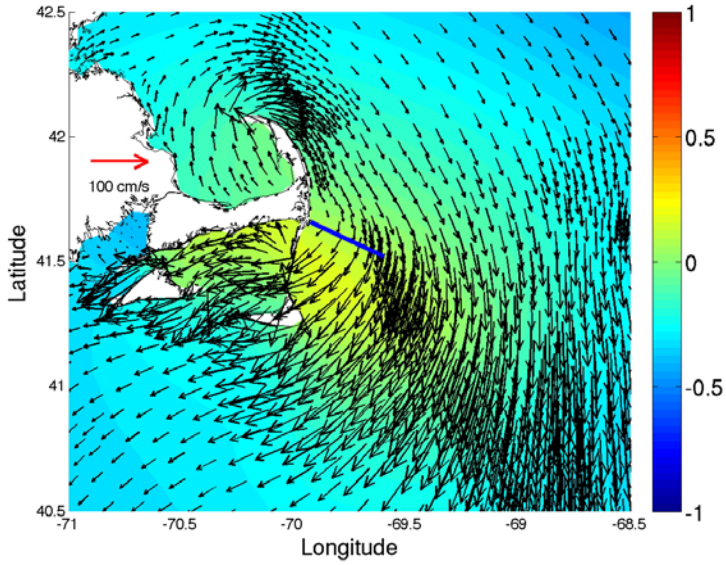

Figure $13c_{-2}$ Model surface current and color-coded sea level (m) at **EBB_{full} +2.17hr** (2012[17] UTC 27 Jan)**.** The blue bar spans stations TTE and NSA.

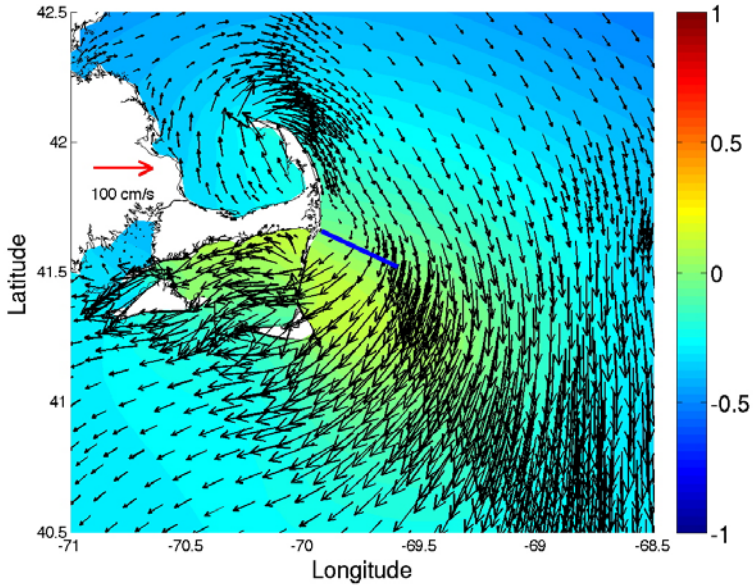

Figure 13c$_{-3}$ Model surface current and color-coded sea level (m) at **EBB$_{full}$+2.37hr** (2022[20] UTC 27 Jan)**.** The blue bar spans stations TTE and NSA.

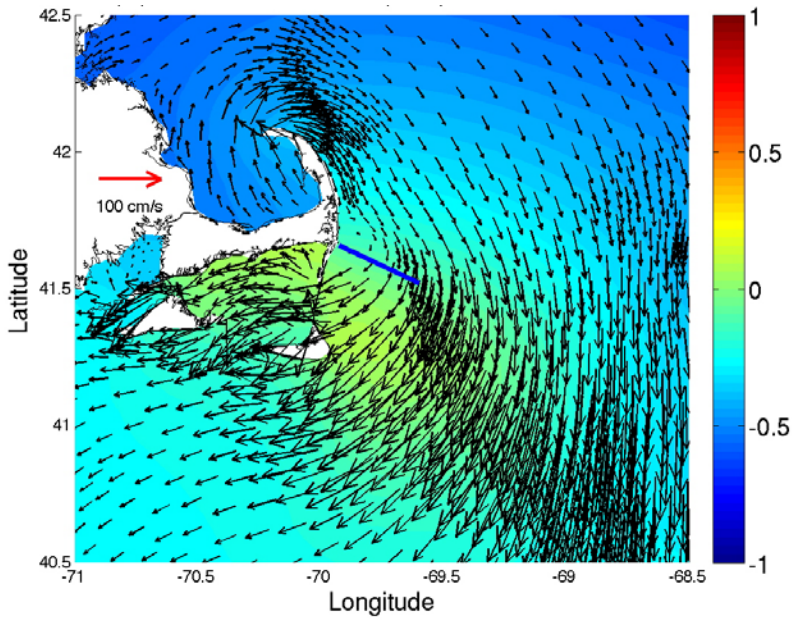

Figure 13c$_{-4}$ Model surface current and color-coded sea level (m) at **EBB$_{full}$+2.55hr** (2032[40] UTC 27 Jan)**.** The blue bar spans stations TTE and NSA.

By 2043 UTC (EBB$_{full}$ +2.72hr), the model surface current maps show distinct CW eddy motion (Figure 13c$_{-5}$).

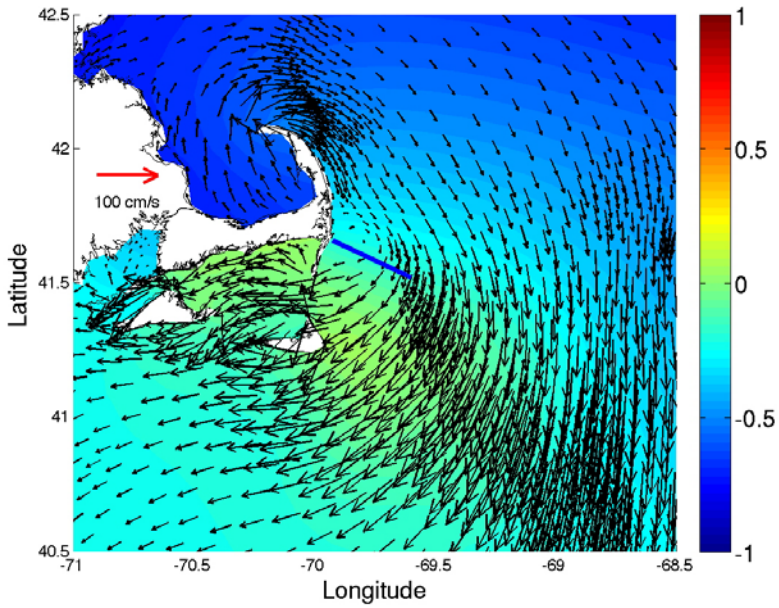

Figure 13c$_{-5}$ Model surface current and color-coded sea level (m) at **EBB$_{full}$ +2.72hr** (2042^{51} UTC 27 Jan)**.** The blue bar spans stations TTE and NSA.

By 2053^{02} UTC (EBB$_{full}$ +2.88hr), the CW eddy motion has begun to translate quickly away from the coast (Figure 13c$_{-6}$).

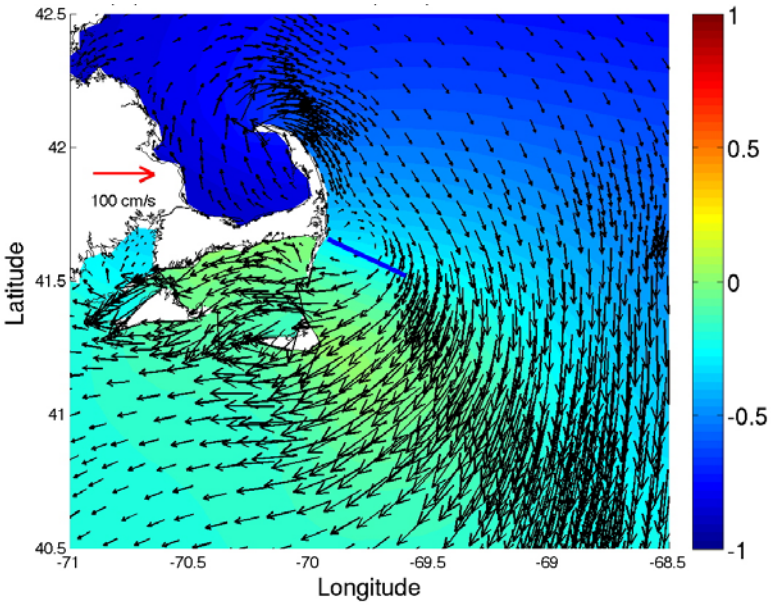

Figure 13c$_{-6}$ Model surface current and color-coded sea level (m) at **EBB$_{full}$+2.88hr** (2053^{02} UTC 27 Jan)**.** The blue bar spans stations TTE and NSA

By 2204 UTC (EBB$_{full}$ +4hr; Figure 13d), the weakening CW eddy motion has translated about 44km offshore toward the southeast.

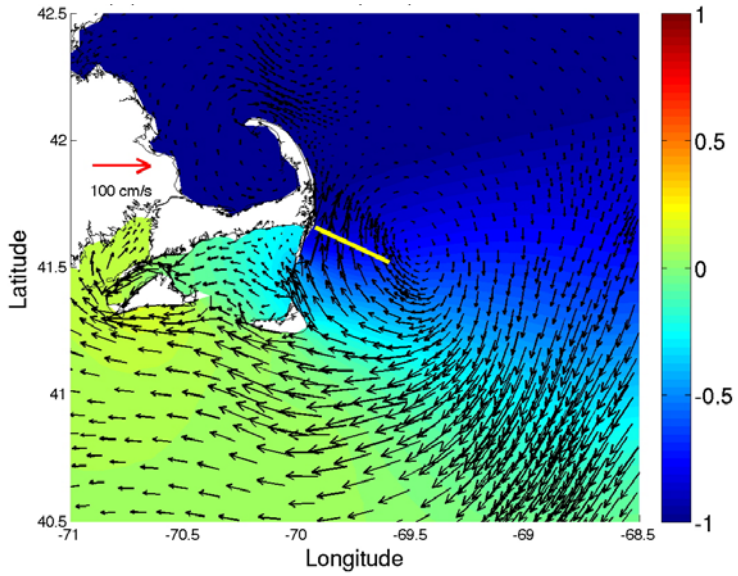

Figure 13d Model surface current and color-coded sea level (m) at **EBB$_{full}$+4hr (**2204[21] UTC 27 Jan**).** The yellow bar spans stations TTE and NSA.

Note that the nearshore arm of the expanding CW eddy motion (Figures 13c and 13d) represents the onset of northward or flood flow along the coast at this time. Then between 2204[21] and 2305[28], the CW eddy motion races across the GSC with the change from ebb tidal flow to flood (Figures 13e) which is complete by 2356.

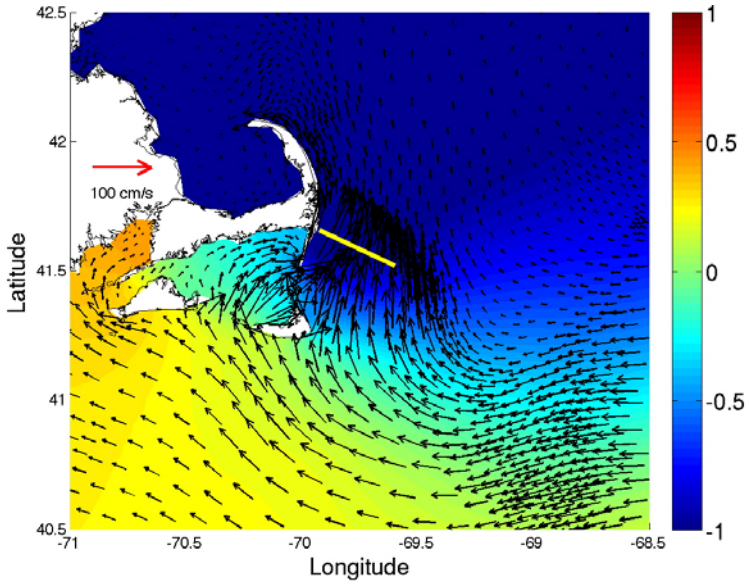

Figure 13e Model surface current and color-coded sea level (m) at **EBB$_{full}$+5hr (**2305[28] UTC 27 Jan**).** The yellow bar spans stations TTE and NSA.

Between 2305[28] UTC (EBB$_{full}$ +5hr) and 0158[39] UTC (EBB$_{full}$ +8hr; Figure 13e), the strengthening northward coastal flow is separates from the coast; creating a near-coast envelope within which ACW motion – the counterpart to the CW eddy motion - will develop within the following hour. The ACW eddy motion evolution and

translation during the flood flow part of the semidiurnal tidal cycle mirrors that of the CW eddy motion in issuing in flood flow across the full GSC.

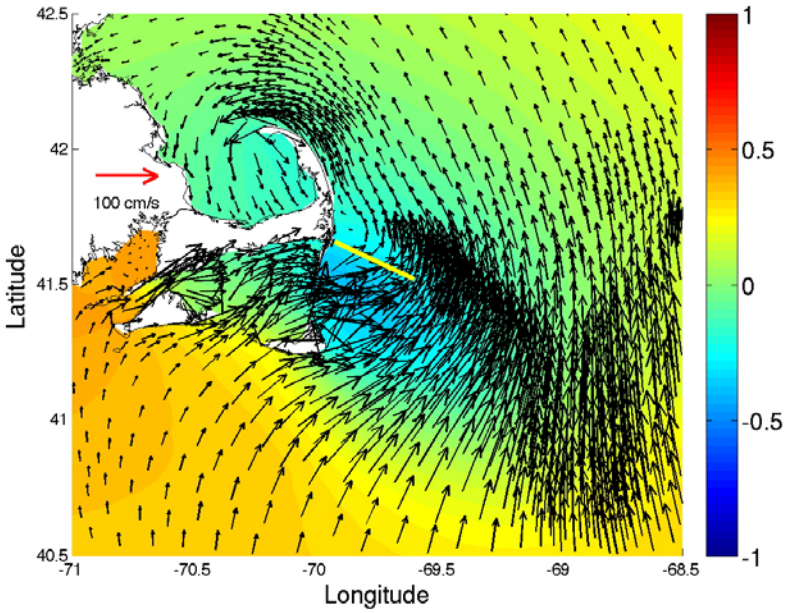

Figure 13f Model surface current and color-coded sea level (m) at **EBB**$_{full}$**+8hr** (0158[39] UTC 28 Jan)**.** The yellow bar spans stations TTE and NSA

During the 2043 to 2204 UTC time period the eddy motion scale is growing. The successive locations of the estimated center of the *model* CW eddy motion (EMC) are shown in Figure 14.

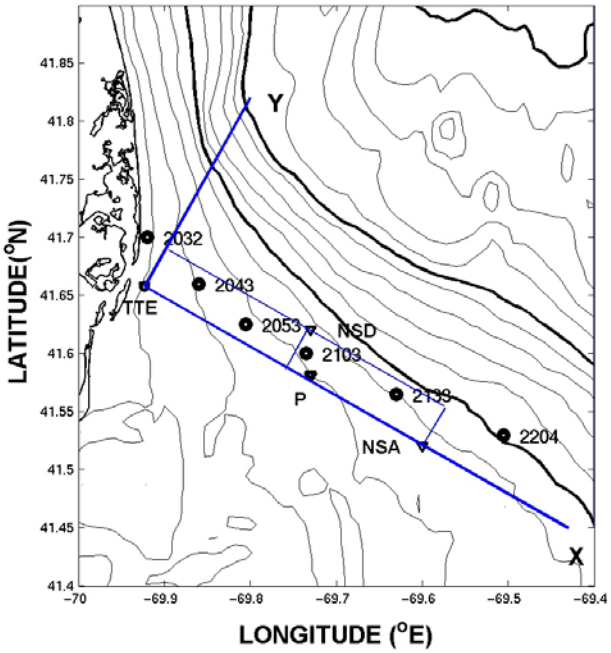

Figure 14 The circles track the *model CW* eddy motion center through the nearshore study region between 2032 and 2204 UTC 27 January 2009. The isobaths are given in 10m intervals from 10m to 100m and then 20m intervals seaward of the 100m isobath.

3. Observation – Model Comparisons

Comparisons between observed and model currents and pressures in this section provided guidance for subsequent exploration of momentum budgets in terms of estimating bottom friction and pressure gradients . The comparison model time series pertain to nodes that were within 4 km of the respective observation stations (see Table 5). Because most of the "observed" currents (except at TTE) were only available by way of 5-tidal constituent hindcasts, all series used in the comparison were 5-tidal constituent hindcasts.

Table 5 The locations and depths of the observation (**-O bold**) and model (-M) station data used in the comparison. The ranges and bearings from the observation sites to the model nodes ("stations") are given along with the effective locations of the large-scale pressure gradients.

Station ID	**Depth** (m)	**Lat** (^{o}N)	**Long** (^{o}W)	**O-M Range** (km)	**O-M Bearing** (^{o}T)
Bottom Pressure					
M1 -O	**184**	**42.07**	**67.87**		
-M	180	42.05	67.87	2.22	180
Mid M1-NAU		***41.94***	***68.90***		
NAU -O	**7**	**41.82**	**69.93**		
-M	50	41.80	69.89	4.00	124
Mid NAU-TTE		***41.74***	***69. 93***		
TTE -O	**13**	**41.66**	**69. 92**		
-M	10	41.67	69. 93	1.39	323
TTE' -M	21	41.63	69. 87	5.33	128
Current					
TTE -O	**13**	**41.66**	**69. 92**		
-M	10	41.67	69. 93	1.39	323
TTE' -M	21	41.63	69. 87	5.33	128
NSA -O	**33**	**41.52**	**69.60**		
-M	40	41.53	69.59	1.39	37
NSD -O	**33**	**41.62**	**69.73**		
-M	50	41.64	69.73	3.34	48
P -O	**30**	**41.58**	**69.73**		
NSB -O	**22**	**41.44**	**69.73**		
NSB -M	23	41.43	69.70	2.74	114

Current Comparisons: The observed and model M_2 tidal current ellipses in Figure 15 have similar orientations, but model currents are clearly more energetic than their observed counterparts. For example, the total current variance at model station NSA (Table 6) is nearly 2 times greater than that for currents at the nearby observation station. This difference prompted us to consider the effect of model bottom friction, which was on a space/time depth-independent bottom current drag coefficient C_d = 0.005. A subsequent model run, with a space/time depth-independent C_d = 0.010, yielded the relatively less energetic model tidal currents in Figure 16. Our practical response to this finding here was to use C_d = 0.010 when estimating bottom stress in selected analyses.

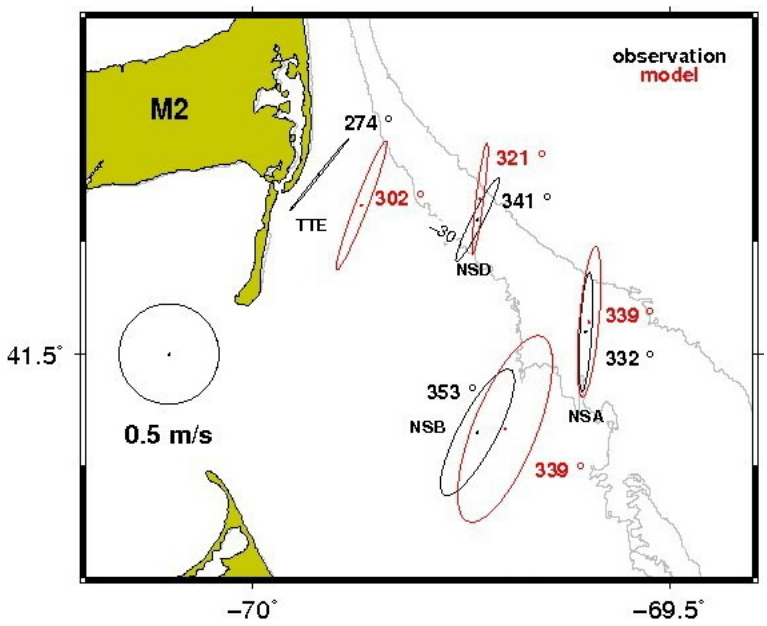

Figure 15 M_2 tidal ellipses for vertically-averaged observed currents at observation stations TTE, NSA, NSB, NSD (blk) and nearby model nodes (red) (see main text). The model currents results were derived from a run in which the model bottom drag coefficient C_d = 0.005. The 30m and 50m isobaths, and the velocity scale are shown.

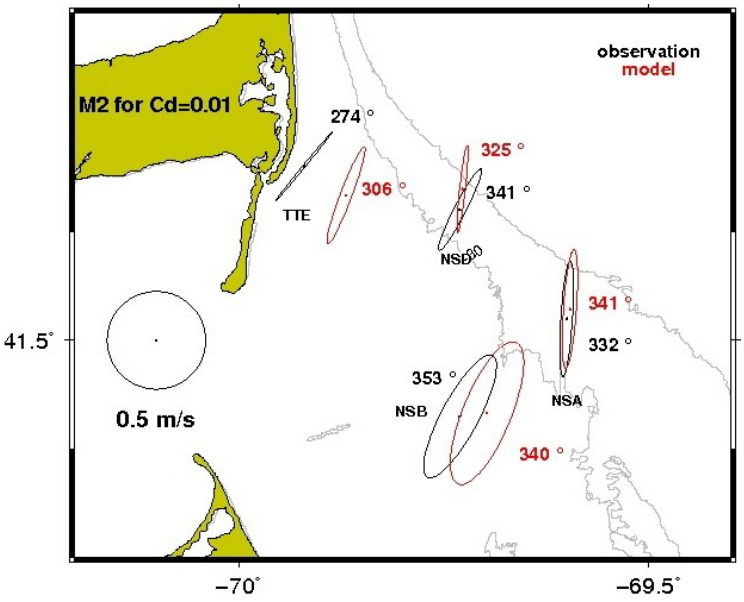

Figure 16 Same as Figure 15, except the model bottom drag coefficient C_d = 0.010.

Bottom Pressure and Pressure Gradient Comparisons: The differences between the model and observed TTE bottom pressure (BP) M_2 harmonic constants are relatively small at -0.2% for the amplitudes and +4^o for the phases, respectively (see Table 7a). The corresponding model minus observation differences for the NAU BPs are +7.2% and +16^o respectively; and somewhat larger than at TTE because of the relatively large depth differences of the observed and model sites (see Table 5).

Table 6 The M_2 constituent harmonic constants at sites at NSD and NSA for the observed (OBS) *rotated (U 120°T; V30°T)* depth-averaged current components (based on 30-day simulation records; also see Appendix A; Tables A3; A4). Harmonic constants are also given for the model (MOD) currents (with drag coefficient C_d = 0.005 and 0.010) at model nodes nearest to the observation sites. The velocity component M_2 harmonic amplitudes and phases in Greenwich epoch are given along with the total current variances. The current ellipses are given in terms of major axis amplitude and orientation, ellipticity (ε=major/minor, with a positive values indicating an anti-clockwise rotating current vectors, and the Greenwich phase of the maximum current.

Station	**Depth** (m)	**M_2 Var** $(cm/s)^2$	**U Amp** (cm/s)	**U Ph** (°G)	**V Amp** (cm/s)	**V Ph** (°G)	**Maj Amp** (cm/s)	**Maj Dir** (°T)	**ε**	**V_{max} Ph** (°G)
OBS										
NSD	33	1074	6.4	226	45.9	341	46.0	27	8	341
NSA	33	1664	26.0	139	51.5	333	57.4	4	-10	330
MOD *(0.005)*										
NSD	50	1553	21.8	150	51.3	319	55.6	7	15	321
NSA	40	2874	32.9	143	68.3	342	75.1	5	-8	339
MOD *(0.010)*										
NSD	50	998	18.2	153	40.8	323	44.6	6	15	324
NSA	40	1874	27.3	149	54.8	344	60.9	4	-9	341

Table 7a M_2 tidal harmonic constants for (1) observed (OBS) BP at TTE from the 57-day record; and at NAU and M1 from Moody et al., (1984); (2) model (MOD) BP at corresponding model stations from the 30-day simulation records; and (3) *Large-Scale* TTE-NAU northward bottom pressure gradient force (PGF_n). Typical analysis uncertainties are given. (See Table A2d for additional details).

	TTE Amp (db)	**TTE Phase** (G°)	**NAU Amp** (db)	**NAU Phase** (G°)	**M1 Amp** (db)	**M1 Phase** (G°)	***Large-Scale* PGF_n Amp** (10^5 x db/m)	***Large-Scale* PGF_n Phase** (G°)
OBS	1.103 ±0.013	119 ± 1	1.032	102	0.782	92	1.894 ±0.080	8 ±2
MOD	1.101 ±0.009	123 ±1	1.109	118	0.859	93	0.576 ±0.002	35 ±0

Table 7b The *model local* PGF_n M_2 harmonic constants based on the 30-day (4 Nov - 4 Dec 2008) records at the indicated stations. Typical analysis uncertainties are given. (See Table A2c for additional details).

NAU Amp (10^5 x db/m)	**NAU Phase** (G°)	**TTE Amp** (10^5 x db/m)	**TTE Phase** (G°)	**TTE' Amp** (10^5 x db/m)	**TTE' Phase** (G°)	**NSD Amp** (10^5 x db/m)	**NSD Phase** (G°)	**NSA Amp** (10^5 x db/m)	**NSA Phase** (G°)
0.448	49	1.063 ±0.003	59 ±0	1.100	69	0.867	64	1.036	88

The differences in the model and observation BP harmonic constants are amplified in the Figure 17 comparison between model-based and observation-based hindcast series. Specifically, the observation-based TTE-NAU bottom pressure difference (PD) amplitude is about 3 times greater than and leads its model counterpart by about 1 hour; as illustrated in the top panel of Figure 17. The TTE-NAU PDs were used to estimate the *large-scale* PGF_n series using the station separations in Table 5. The *large-scale* TTE-NAU PGF_n series are the exact spatial averages, which technically are located midway between NAU and TTE.

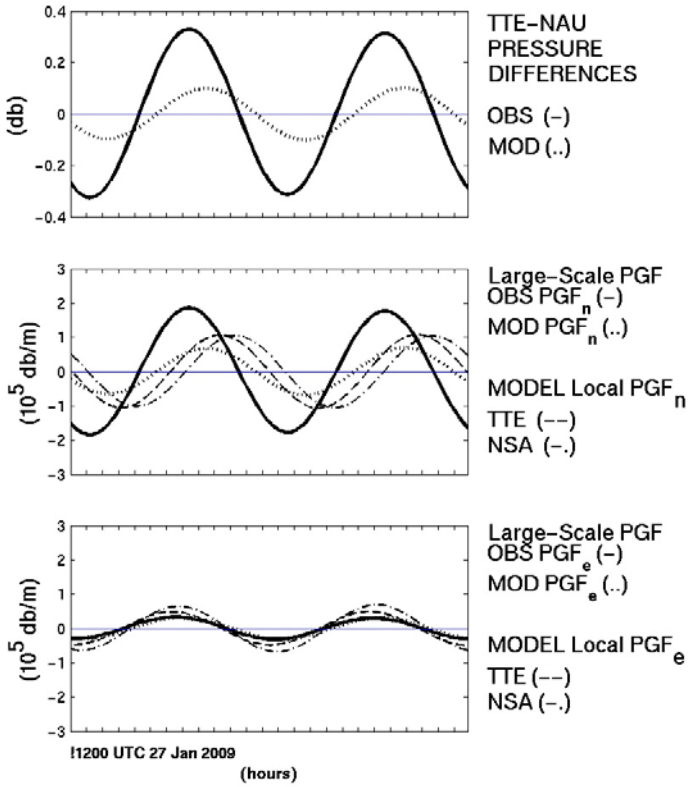

Figure 17 *Observed (-) and model (…)* 5-tidal constituent hindcast time series of the **(upper)** TTE-Nauset bottom pressure difference (PD); **(middle)** *Large-Scale* northward pressure gradient force PGF_n (..) and *model Local* PGF_n *(-)* at TTE (--) and NSA (-.); and **(bottom)** eastward pressure gradient forces.

The *large-scale* PGF_n time series do not compare very well with the *local model* PGF_n time series. Specifically, the hindcast observed *large-scale* PGF_n time series is about 1.3 times greater in amplitude and leads by 2 hours the model *local* PGF_n time series at station TTE; as indicated in the middle panel of Figure 17. The structure of the model *local* PGF_n time series is illustrated in terms of its M_2 harmonic constants (Table 7b), which show that (1) PGF_n amplitudes are relatively uniform (~ 1.0 x 10^5 x db/m) throughout the study region; (2) PGF_n phases generally lag going southeastward across the study region, and (3) PGF_e amplitudes and phases are smaller and uniform throughout the study region.

We conclude from these comparisons that the *large-scale* pressure gradient estimates are too large and too early (+2-3 hours) to be used effectively for local dynamics considerations considered below. Therefore, for all subsequent analyses presented in this paper, *model local pressure gradient* time series are employed.

4. Eddy Motion Kinematics: 27 January 2009 Time Series

The following analysis of the model current and pressure time series from station near our observation stations reveals the presence of a robust eddy motion formation

and evolution process. A similar analysis of the observations that follows confirms the basic conclusions of this analysis.

A. Analysis of Model Results

We first diagnose the 27-28 January 2009 segments of the model hindcast pressure and current hindcast series (see Figure 18). These hindcast series were based on 20 of the classically most important astronomical tidal constituents plus several of the most important hydrodynamics-induced higher harmonic constituents, namely M_4, M_6, S_4, and S_6.The harmonic constants result from a tidal harmonic analysis of the series produced by the model run with $C_d = 0.005$. The details of the eddy motion formation and evolution process, which were inferred from inspection of Figures 13 and 18, are summarized in Table 8.

Table 8 Transient tidal eddy motion formation and evolution – 27-28 January 2009. The milestones are referenced to **EBB_{full}** or 1800 UTC – the time of maximum ebb flow throughout the Great South Channel (GSC) region. Reference is made to the status of the Coastal boundary Layer (CBL), the eddy motion center (EMC), and increases (inc) and decreases (dec) in intensity.

Time (GMT)	**Time** rel **EBB_{full}** (hr)	**Model Tidal Stage**	**Eddy Motion Formation & Evolution Process**
1558	-2.03	GSC flood decrease CBL ebb increase	ACW EMC/vorticity max translates SEward w/ intensity dec. and scale inc.
1659	-1.02	weak GSC flow eastward CBL ebb increase	Decreasing ACW EMC/vorticity max translates to central GSC
1800	+0.00	**EBB_{full}** - full GSC ebb flow -	ebb_{max} – *Inner Zone* $pgf_y \sim 0$
1901	+1.02	CBL ebb decrease GSC ebb	ebb_{max} – *Outer Zone* pgf_y inc - CBL ebb separation onset
2002	+2.03	CBL ebb decrease GSC ebb	pgf_y inc
2033	+2.55	CBL ebb stalls GSC ebb	pgf_y inc - CBL ebb separation
2042	+2.70	CBL flow reverses GSC ebb	**CW eddy motion forms near the coast**
2053	+2.88	CBL flood flow onset GSC ebb	CW EMC traverses *Inner Zone*
2103	+3.05	CBL flood flow estab. GSC ebb	*Inner Zone* pgf_{ymax} vorticity minimum - CW EMC enters *Outer Zone*
2204	+4.07	CBL flood decreasing GSC ebb	pgf_{ymax} CW EMC traverses *Outer Zone*
2305	+5.08	CBL flood separation onset weak GSC flow westward	pgf_y dec decreasing CW EMC/vorticity min in central GSC
0006	+6.10	**$FLOOD_{full}$** - full GSC ebb flow -	$flood_{max}$ – *Inner Zone* pgf_y dec
0107	+7.12	CBL flood separation GSC flood	$flood_{max}$ – *Outer Zone* pgf_y reversal -
0159	+7.98	near-coast flood stalls GSC flood	(- pgf_y) inc
0300	+9.00	CBL ebb flow estab. GSC flood	**ACW eddy motion forms near the coast**

The study region lateral V current difference time series represents the clearest signature of the eddy motion formation and evolution in the study near coast study region, as explained next. This can be seen by considering the formation and evolution of CW ebb flow eddy motion; as seen in Figures $13c_{-1}$ and $13c_{-2}$ and detailed in Table 8. The nominal beginning of the formation of CW eddy motion is at about 1800 UTC on 27 January 2009 near the coast. At that time three events are occurring, namely (a) the *Inner Zone (IZ)* Y-pressure gradient force transitions from negative to positive (see pgf_y in Figure 18 - panel 1); (b) the *IZ-averaged* ebb flow begins to accelerate from its minimum (i.e. a slowing of –V; see V in Figure 18 - panel 2); and (c) the *Outer* minus *IZ* lateral V difference (due primarily to the phase difference) transitions from positive to negative (see O-I del_xV; Figure 18 - panel 3). For about 2½ hours between 1800 and 2032, both the O-I del_xV and study region-average vorticity (i.e., AVERAGE estimated $\approx \delta v/\delta x - \delta u/\delta y$ - see Figure 18; panel 4) continue to decrease – consistent with as the formation of distinct CW eddy motion within the CBL envelop near the coast.

For the next 1½ hours between 2032 and 2204, the lateral scale of the of the CW eddy motion grows more rapidly with the associated migration of the eddy motion center (EMC) across the 30km study region at a rate of about 5 m/s (Figure 14); and consistent with the Figure 18 time series. More specifically during this interval, the strong negative in the *IZ* $\delta_x V$ (= $V_P - V_T$) signal at 2103, which is due to weak positive V at station TTE and relatively strong negative flow at station P, signals CW eddy motion formation nearshore . This is consistent with the model picture in Figure $13c_{-6}$ at 2042 UTC (or EBB_{full}+2.7hr) – a few minutes earlier.

Then at about 2204 the CW eddy motion leaves the near-coast study region, with the corresponding increase in O-I del_xV and study region depth-averaged vertical vorticity (estimated $\approx \delta v/\delta x - \delta u/\delta y$ - see Figure 18; panel 4).

The signature of the transient tidal eddy motion is not as clear in the vorticity because regional vorticity is affected by flow processes in addition to that of the transient tidal eddy motion. Nevertheless, we find that a strong *IZ* vorticity minima that coincides with nearshore beginnings of CW eddy motion at 2042 (EBB_{full}+2.7hr in Table 8 and Figure 18; panel 4), as described above. The *local IZ* vorticity decreases (i.e., weakens) during the following 2 hours between EBB_{full}+3hr and EBB_{full}+5hr. Simultaneously, the weakening CW eddy pattern is growing in scale as the EMC translates with increased speed (~ 28 m/s) southeastward (more or less along the isobaths) across the GSC. By 2400^+ (0^+ hours on 28 Jan; $EBB_{full}+6^+$hr), the CW eddy motion pattern disappears as the ingoing flood tidal flow fills the whole GSC at $FLOOD_{full}$.

$FLOOD_{full}$ marks the time when the corresponding cycle for the ACW eddy motion begins. Within about 2 ½ hours (at ~ 0230 UTC 28 Jan), the ACW eddy motion becomes well defined near the coast in the model pictures. It too grows in scale near coast over the next ~ 1 ½ hours and leaves the coast to cross the GSC with the full onset of ebb tidal flow – nearly mirrowing the CW eddy motion formation and evolution.

However, the model results indicate that the ACW eddy motion is slightly stronger than the CW eddy motion. This can be seen in the approximately 5% asymmetry in the O-I $del_x V$ and AVERAGE vorticity time series records in Figure 18. Kinematically this result derives from the hydrodynamically-induced asymmetry in the model (and real) ocean fields. In our companion paper (GB11), the implications of this asymmetry in terms of secondary flow upwelling/downwelling is explored. Here we continue by exploring what the observation based results show concerning the kinematics of the eddy motion process.

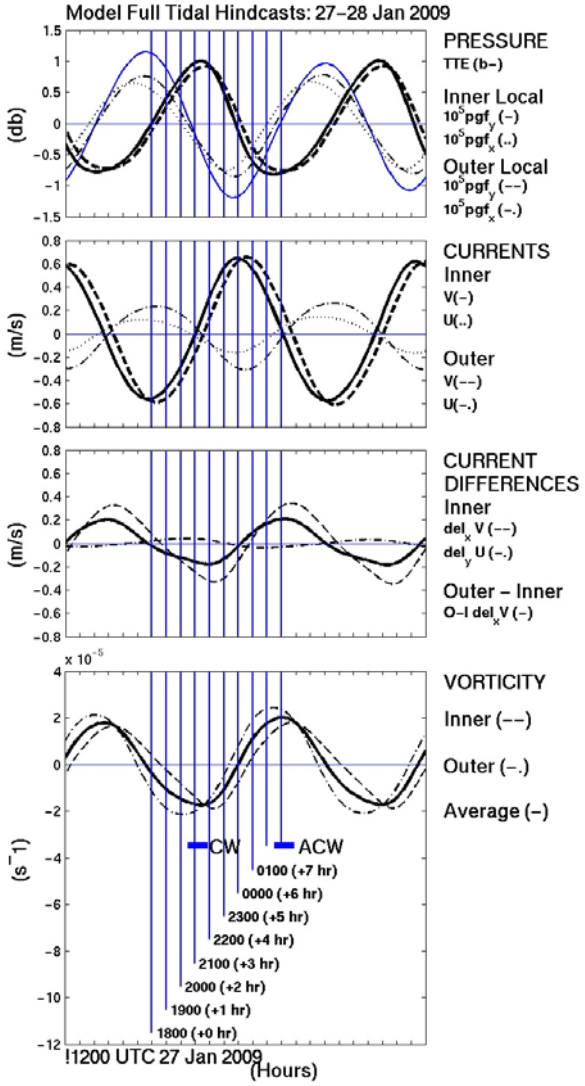

Figure 18 Full tidal hindcasts of *model* **(top panel)** TTE bottom pressure and local pressure gradient force components (pgf_y, pgf_x) in the *Inner and Outer Zones* (see text) ; **(2nd panel)** *Inner and Outer Zone*-averaged current component records; **(3rd panel)** *Inner Zone* $\delta_x V$, Outer-Inner Zone $\delta_x V$, and $\delta_y U$ current-difference records; and **(bottom panel)** *Inner and Outer Zone* vorticity estimates. The hourly milestones in the flow kinematics and the durations of the CW and ACW eddy motion in the study region are indicated (see Figures 13 and Table 8).

B. Analysis of Observation Results

The observation-based results, which are given in terms of a set of 5-tidal constituent hindcast series in Figure 19 are basically consistent with the model-derived results in Figure 18. However there are differences; *first* because the observation-based velocities are relatively weaker than model velocities (as discussed above); and *second* because the observation-based hindcast series results lack the hydrodynamically-induced asymmetries of their model counterparts (compare Figures 18 and 19). The lack of asymmetries is most obvious in the 5-tidal constituent hindcast current differences, vorticities and local *model* pressure gradient series.

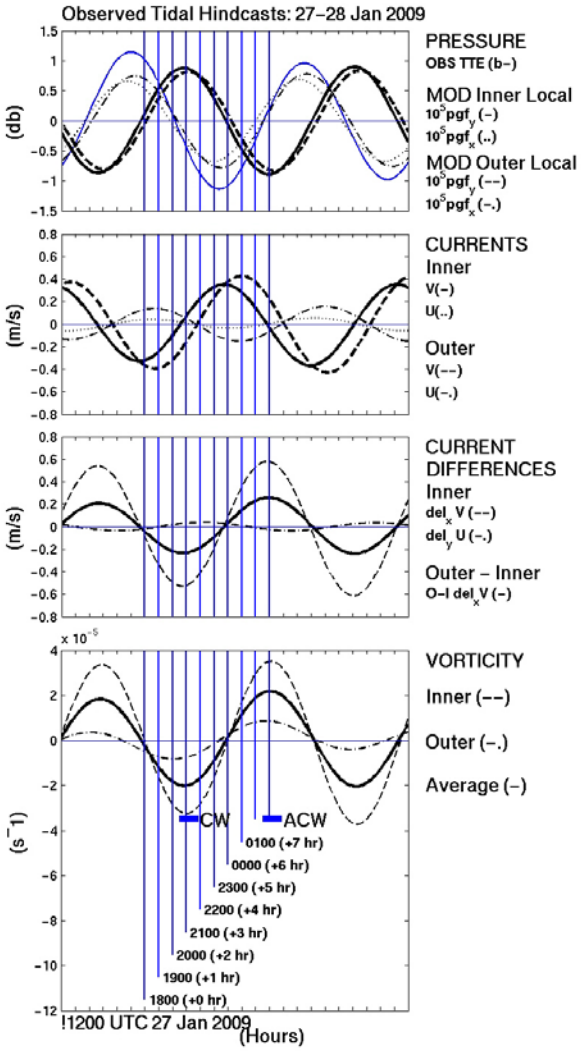

Figure 19 Five-constituent tidal hindcast **(top panel)** model *local* pressure gradient force components (pgf_y, pgf_x) in the *Inner and Outer Zones* (see text) as well as the TTE bottom pressure; **(2nd panel)** *Inner and Outer Zone*-averaged current component records; **(3rd panel)** *Inner Zone* $\delta_x V$, Outer-Inner Zone $\delta_x V$, and $\delta_y U$ current-difference records; and **(bottom panel)** *Inner and Outer Zone* vorticity estimates. The hourly milestones in the flow kinematics and the durations of the CW and ACW eddy motion in the study region are indicated (see Figures 13 and Table 8).

The similarities of the observed and model results include the basic timing of all of the variables and particularly the study regional current difference and vorticity series. Interestingly the phase differences between modeled and observed currents almost compensates for the large model-observation amplitude differences in producing the current differences; with the model current difference amplitude being slightly smaller. There are also some larger amplitude differences in *Inner and Outer Zone* series.

C. Summary

The process revealed by the above evidence suggests that it is a forced tidal vorticity wave originates in shallow water in terms of alternating CW and ACW eddy motions, which translate across the GSC - communicating information about the change from ebb-to-flood and flood-to-ebb tidal flows, respectively. Shortly after either maximum ebb or flood flow in the Great South Channel (GSC), the CW or ACW eddy motion formation process begins in the shallow water just offshore from Chatham, MA. For CW eddy motion at that time, the alongcoast pressure gradient force begins to slow the prevailing ebb tidal flow; and both of the regional lateral V difference (O-I del_xV) and vorticity time series transition from positive to negative. During the next 2 ½ hours the negative vorticity CW eddy motion grows within a bulge in the coastal boundary layer (CBL); with a consistent decrease in the regional vorticity (and O-I del_xV). Finally, with coastal boundary layer (CBL) separation, the eddy motion leaves the near coast study region and rapidly traverses across the GSC completing the change from ebb to flood tidal flow in the GSC region. The converse of the above scenario is seen in the formation and evolution history of the ACW eddy motion during the flood tidal flow half tidal cycle

The dynamics of this process are explored next.

5. Eddy Motion Dynamics

In this section, estimates of the terms in the conservation of momentum and vorticity equations derived from measurements are compared with corresponding model-derived estimates. The framework for that comparison is the following vector form of the momentum equations:

$$\frac{D\vec{u}}{Dt} = \frac{\partial \vec{u}}{\partial t} + \vec{u} \bullet \nabla \vec{u} + \vec{f} x \vec{u} = -\frac{1}{\rho} \nabla p + \frac{1}{\rho} \left[\nabla \bullet \vec{\vec{\sigma}} \right] \quad , \qquad (1)$$

where $\vec{u} = u\vec{i} + v\vec{j} + w\vec{k}$ is total velocity, f is the Coriolis parameter, ρ is water density, p is pressure, and $\vec{\vec{\sigma}}$ is the stress tensor. For the case of external tidal variability in the Gulf of Maine, Brown (1984) neglects (1) stratification effects and (2) lateral stresses relative to bottom stresses (assuming that surface stress τ^s is zero) in producing the

volume-averaged components of the momentum equations for a shallow-water study region with an area $A = \Delta x \Delta y = (x_2 - x_1)(y_2 - y_1)$. The components are in the:

X-direction

$$\frac{\rho_o}{A}\left\{\left[\frac{\delta u}{\delta t}\right] + \left\langle \delta_x \overline{uu} \right\rangle_y + \left\langle \delta_y \overline{uv} \right\rangle_x - f[v] + \frac{1}{\rho_o}\left\langle h \frac{\partial p_b}{\partial x} \right\rangle\right\} = RES_x = -\frac{1}{A}\left\langle \tau_x^b \right\rangle + error \qquad (2a)$$

Y-direction

$$\frac{\rho_o}{A}\left\{\left[\frac{\delta v}{\delta t}\right] + \left\langle \delta_x \overline{uv} \right\rangle_y + \left\langle \delta_y \overline{vv} \right\rangle_x + f[u] + \frac{1}{\rho_o}\left\langle h \frac{\partial p_b}{\partial y} \right\rangle\right\} = RES_y = -\frac{1}{A}\left\langle \tau_y^b \right\rangle + \frac{1}{A}\left\langle \delta_x h T_y \right\rangle_y + error, \qquad (2b)$$

inertial nonlinear Coriolis pressure gradient bottom stress lateral stress

where ρ_o is the reference water density (1025.7 kg m^{-2}), p_b is bottom pressure, τ^b is the bottom stress, and T_y is the vertically-averaged Y-directed lateral stress on the water. The notation for the different integrals and differences are

$$\overline{.....} \equiv \int_{-h}^{\eta} .....dz \quad ; \quad [.....] \equiv \int_{y1}^{y2}\int_{x1}^{x2}\int_{-h}^{\eta} .....dxdydz \; ; \quad \langle .... \rangle \equiv \int_{y1}^{y2}\int_{x1}^{x2} .....dxdy \; ; \quad \langle .... \rangle_y \equiv \int_{y1}^{y2} .....dy \; ;$$

$$\langle .... \rangle_x \equiv \int_{x1}^{x2} .....dx \; ; \quad \delta_x f(x,y) = f(x_2) - f(x_1) \text{ , and } \delta_y f(x,y) = f(y_2) - f(y_1) \; .$$

A. Observed Inner Zone Momentum Budgets

The volume-averaged momentum budgets in the shallower *Inner Zone* (*IZ*; with mean depth ~23m) were explored first. We estimated the terms left-hand-side (LHS) of Eq (2) using the algorithms presented in the Appendix B Table B3b - with the appropriate tidal hindcast velocity and *model* C_d = 0.005-local pressure gradient series as discussed above. The energetic set of *IZ* Y-momentum term time series (Figure 20; Table 9) features a first order balance between the pressure gradient (PG_y^{005}) and the combined local acceleration ($INERTIAL_y$) and $-RES^{nf}$ terms. The $CORIOLIS_y$ and $NONLINEAR_y$ terms make considerably less contributions to the Y-momentum budget.

The *Inner Zone* X-momentum time series budget (Figure 20) features a first order balance between PG_x and a combination of the $CORIOLIS_x$ and $-RES^{nf}_x$ terms; with insignificant contributions from $INERTIAL_x$ and $NONLINEAR_x$. This case clearly demonstrates the role of $CORIOLIS_x$ in turning the velocity vector through the sharp ACW turns of the tidal current ellipse extrema (see Figure 10). In particular near V_{max}, the negative $CORIOLIS_x$ is slowly turning V (which is slowing due to a $-PG_y$) toward the west through its ACW elliptical path.

The RES^{nf}_x and RES^{nf}_y component series are the respective sums of the Eq 2 LHS terms; which of course would be zero for an exact balance. In reality the RES series are not zero, but rather sums of (a) disregarded terms – e.g., bottom stress and lateral momentum diffusion, (b) estimation algorithm inaccuracies, and (c) hindcast input series uncertainties. Never-the-less the $-RES^{nf}$ series close the respective component momentum budgets exactly.

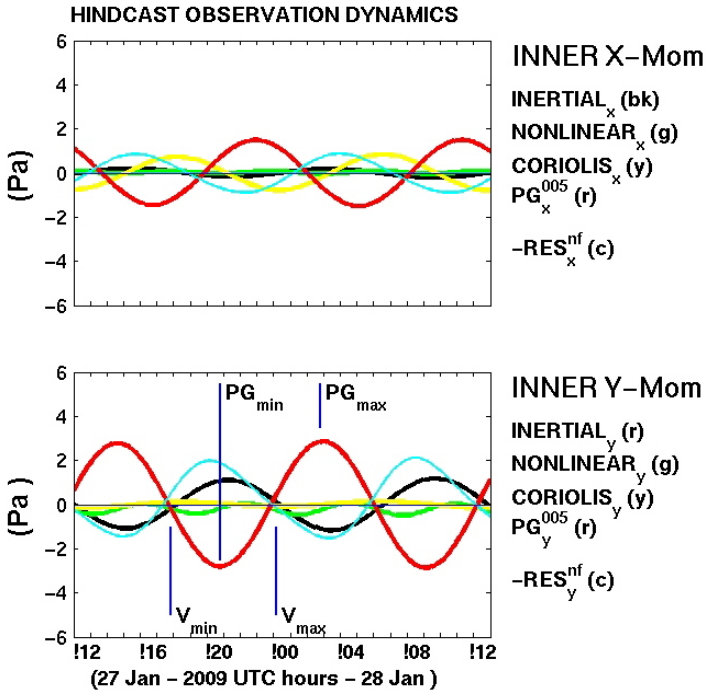

Figure 20 The **observed** *Inner Zone* momentum term estimates (in Pascals) for the (**upper**) X-direction and (**lower**) Y-direction. The model PGs for $C_d = 0.005$ are used. The negative RES terms balance the momentum budget by definition. V and PG extrema times are indicated.

In the second round of momentum budget estimates, we assumed that bottom stress terms must contribute significantly to the RES^{nf}_y and RES^{nf}_x terms in such shallow water. Thus, we estimated bottom stress explicitly using the same quadratic bottom stress algorithm as the model at each station. The algorithm for the x-directed bottom stress estimate at station TTE is

$$\tau^{\,b}_{x} \;=\; \rho_o C_d \left(\sqrt{\left(u^{\,bot}_{TE}\right)^2 + \left(v^{\,bot}_{TE}\right)^2} \right) u^{\,bot}_{TE} \qquad , \qquad (3)$$

where C_d is the bottom drag coefficient and $u^{bot}_{TE}; v^{bot}_{TE}$ is the bottom current. Based an inspection of the model current profiles in the study region, we estimated the bottom current amplitudes at a station to be 60% of the local depth-averaged currents and in phase. Based on the better model versus observed current ellipse comparisons in Figure 16, a $C_d = 0.010$ was used for the observation-derived bottom stresses. The spatially-averaged *IZ* bottom stresses are simple averages of the respective local quadratic bottom stress estimates at station TTE and P (see Appendices B3 & B4 for details). The *OZ* spatially-averaged, bottom stresses derive from stations NSA and

NSD bottom stress estimates. To be more dynamically consistent, we also used the model local pressure gradients from the model run with $C_d = 0.010$.

These $C_d = 0.010$-based *Inner Zone* momentum budget results (Figure 21) show a significant reduction in the RES variance relative to the average term variance (see Table 9). Specifically, the Relative RES_y Variance (RRV), which we define as RRV=100 x (RES_y – Average Term Variance or ATV) / ATV, decreased from $RES_y^{nf} \sim +20\%$ to $RES_y^{01} \sim +8\%$. The reduction in relative RES_x variance was even better – reduced from ~+3% to ~-20%.

In an effort to reduce RRV even further, we explicitly estimated the lateral stress term (see Eq 2b) in the *Inner Zone*. Vertically-averaged lateral stress was parameterized as

$$T_y = \rho_o L_D \left[\left(\bar{v}\right)^2 / h^2 \right], \qquad (4)$$

where L_D is the lateral "drag coefficient". This term was estimated using the algorithms in Appendix B, with the very conservative assumption that $L_D = 1$ (probably on the high side). Even with this approach, the lateral stress estimate amplitude was found to be very small (see OBS-3 column in Table 9) and, because of phase differences, actually increased the RRV. Thus, we concluded that lateral stress variability was insignificant and was not considered further as we moved on to consider momentum budgets in the *Outer Zone*.

Table 9 The rms amplitudes and variances of the *Inner Zone* X-Y momentum term time series for several scenarios.

Momentum Budget Terms (Pascals)	**OBS -1** $C_d = 0.005$ mPG (C_d=0.005)		**OBS -2** $C_d = 0.01$ mPG (C_d=0.01)		**OBS -3** $C_d = 0.01$ mPG (C_d=0.01) $C_L = 1$	
	AMP	VAR	AMP	VAR	AMP	VAR
INNER-X						
Inertial	0.130	0.017	0.130	0.017	0.130	0.017
Advective	0.039	0.002	0.039	0.002	0.039	0.002
Coriolis	0.557	0.310	0.557	0.310	0.557	0.310
Pressure Grad	*1.050*	*1.103*	*0.845*	0.714	*0.845*	0.714
Bottom Stress	-		0.061	0.004	0.061	0.004
Lateral Stress	-		-		0.038	0.001
RESIDUAL	0.611	0.373	0.400	0.160	0.404	0.163
Average		0.361		0.201		0.173
RRV		**+ 3.3%**		**-20.3%**		**-5.8%**
INNER-Y						
Inertial	0.798	0.636	0.798	0.637	0.798	0.637
Advective	0.174	0.030	0.174	0.030	0.174	0.030
Coriolis	0.094	0.009	0.094	0.009	0.094	0.009
Pressure Grad	*1.984*	*3.936*	*1.568*	*2.459*	*1.568*	*2.459*
Bottom Stress	-		0.398	0.158	0.398	0.158
Lateral Stress	-		-		0.094	0.009
RESIDUAL	1.209	1.462	0.851	0.724	0.874	0.764

Average	1.215	0.669	0.581
RRV	**+20.3%**	**+ 8.3%**	**+31.4%**

B. Observed Outer Zone Momentum Budgets

The *Outer* Zone Y-momentum budget results (C_d=0.01; see Figure 22; Table 10) featured a principal dynamic balance between the C_d=0.01 model-derived local pressure gradient and the inertial term which was more robust than its *IZ* counterpart; due to the generally stronger *OZ* flows. The *OZ* bottom stress (BSF_y^{01}) term was about 25% larger than its *IZ* counterpart and more in phase with the *OZ* average current than was its IZ counterpart, the amplitude of the -RES^{01} term was relatively smaller.

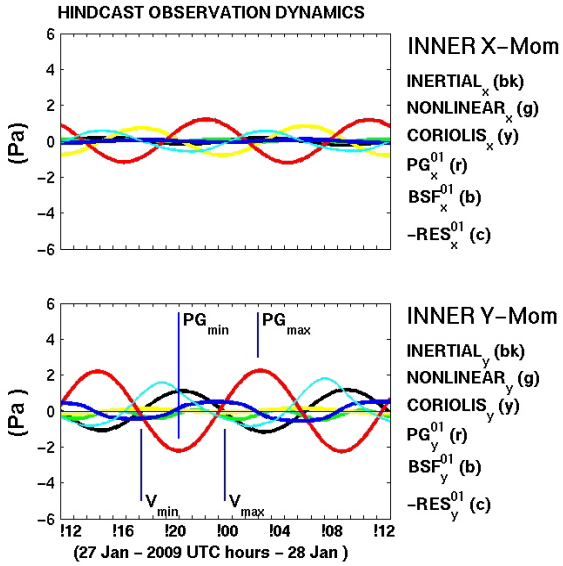

Figure 21 The **observed** *Inner Zone* momentum term estimates (in Pascals) for the (**upper**) X-direction and (**lower**) Y-direction; with bottom drag coefficient C_d = 0.01 and the model PGs for C_d = 0.01. The negative RES^{01} terms balance the momentum budget by definition. V and PG_y extrema times are indicated.

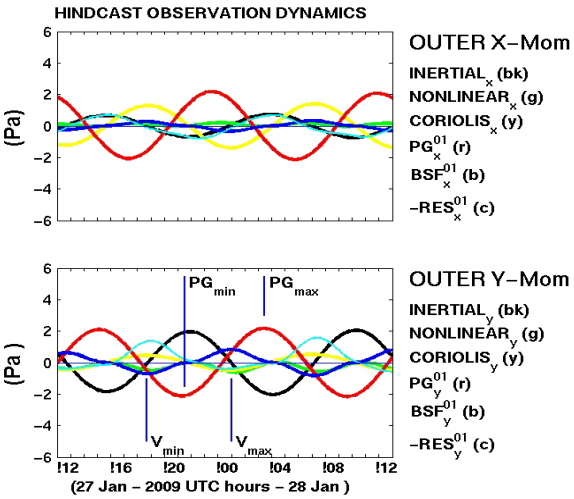

Figure 22 The **observed** *Outer Zone* momentum term estimates (in Pascals) for the (**upper**) X-direction and (**lower**) Y-direction; with C_d = 0.01 and the model PGs for C_d = 0.01. The negative RES terms balance the momentum budget by definition. V and PG_yextrema times are indicated.

Table 10 The rms amplitudes and variances of the *Outer Zone* X-Y momentum term time series for several scenarios.

Momentum Budget Terms (Pascals)	**OBS-1** C_d = 0.005 mPG (C_d =0.005)		**OBS-2** C_d = 0.01 mPG (C_d =0.01)		**OBS-3** C_d = 0.01 mPG (C_d =0.01) C_L = 1	
	AMP	VAR	AMP	VAR	AMP	VAR
OUTER-X						
Inertial	0.495	0.245	0.495	0.245	0.495	0.245
Advective	0.073	0.005	0.073	0.005	0.073	0.005
Coriolis	0.958	0.919	0.958	0.919	0.958	0.919
Pressure Grad	*1.796*	3.224	*1.502*	*2.255*	*1.502*	*2.255*
Bottom Stress	-		0.188	0.035	0.188	0.035
Lateral Stress	-		-		0.038	0.001
RESIDUAL$_x$	0.821	0.675	0.482	0.232	0.482	0.232
Average		1.014		0.615		0.527
RRV		**-33.4%**		**-62.3%**		**-56.1%**
Inertial	1.385	1.919	1.385	1.919	1.385	1.919
Advective	0.197	0.039	0.197	0.039	0.197	0.039
Coriolis	0.343	0.118	0.343	0.118	0.343	0.118
Pressure Grad	*1.845*	*3.402*	*1.493*	*2.230*	*1.493*	*2.230*
Bottom Stress	-		0.478	0.229	0.478	0.229
Lateral Stress	-		-		0.268	0.072
RESIDUAL$_y$	0.540	0.292	0.635	0.404	0.757	0.574
Average		1.154		0.823		0.740
RRV		**-74.7%**		**-50.9%**		**-22.5%**

C. Observation Versus Model Momentum Budget Comparisons

Here we report on comparisons of *Outer Zone* observation-based and model-based momentum budgets for which different C_ds were used. These comparisons were conducted in a standard earth-based (E-N) coordinate system so that the results could be compared with other published results later. (While not explicitly detailed here, appropriate adjustments were made to the geometry of the volume-averaging algorithms). As expected with just a relatively small orientation difference, the characteristics of the *Outer Zone* observation-derived C_d = 0.010 momentum budgets in the E-N frame of reference (Figure 23; Table 11) are very similar to those of the X-Y frame (Figure 22; Table 10). (Note C_d = 0.010-momentum budgets are *defined* as those based on a C_d = 0.010 bottom stress estimate plus the use of the model pressure gradients derived with a C_d = 0.010 bottom stress).

However, the *Outer Zone* observation-derived C_d = 0.005-momentum budgets in Figure 24 are significantly more energetic than the C_d = 0.010-momentum budgets (Figure 23) because with less bottom stress, the former is characterized by relative larger currents and

pressure gradients. The differences are seen in the larger average momentum term variances of the $C_d = 0.005$-momentum budgets.

Table 11 The rms amplitudes of the E-N momentum term time series for several scenarios.

Momentum Budget Terms (Pascals)	**OBS-1** mPG-C_d=0.005 C_d = 0.005		**OBS-2** mPG-C_d=0.01 C_d = 0.01		**QUODDY** C_d = 0.005	
OUTER-E						
Inertial	0.267	0.071	0.267	0.071	0.222	0.049
Advective	0.082	0.007	0.082	0.007	0.118	0.014
Coriolis	1.001	1.002	*1.001*	*1.002*	*1.504*	*2.262*
Pressure Grad	*1.506*	*2.268*	*1.231*	*1.515*	*1.506*	*2.268*
Bottom Stress	0.039	0.001	0.077	0.006	0.034	0.001
RESIDUAL	0.716	0.513	*0.506*	*0.256*	*0.170*	*0.029*
Average		0.644		0.476		0.771
RRV		**-20.3%**		**-46.2%**		**-96.2%**
Inertial	1.447	2.093	*1.447*	*2.093*	*2.160*	*4.664*
Advective	0.143	0.020	0.143	0.205	0.120	0.145
Coriolis	0.184	0.034	0.184	0.034	0.154	0.023
Pressure Grad	*2.080*	*4.325*	*1.714*	*2.938*	*2.080*	*4.325*
Bottom Stress	0.254	0.064	0.508	0.258	0.557	0.311
RESIDUAL	0.751	0.563	*0.603*	*0.364*	*0.211*	*0.045*
Average		1.183		0.982		1.586
RRV		**-52.4%**		**-62.9%**		**-97.1%**

How do the observation-based C_d = 0.005-momentum budgets compare to the corresponding QUODDY momentum budgets in Figure 25 (see Table 11) The answer is that they are very similar - both visually and quantitatively () -, except for the $CORIOLIS_e$, $INERTIAL_n$, and both RES terms. The exceptions: the model -RES terms are very small because as one would expect, the model momentum terms based on a dynamically self-consistent set of model variables should balance. The non-zero RES amplitudes are very small and in this case are quantitative measures of our aggregated term algorithm inaccuracies.

Finally, how do the MB11 model dynamics compare with the He and Wilkin (2006; or HW06) model results, which the authors extracted from their C_d= 0.005 model run at station "C" (located in Figure 9 in about 35m of water)? They compare very well in terms of amplitude and phase of virtually all the terms. Like our observation-based results (Figure 25;Table 11), the HW06 model N-S momentum budget (Figure 26) features a dominant pressure gradient that is balanced primarily by the inertial term; with small contributions from bottom stress (C_d= 0.005) and nonlinear-terms. For both models, the primary E-W momentum balance is between the pressure gradient and Coriolis terms; with very small contributions from the inertial, bottom stress, and nonlinear-terms.

Summarizing the results of these comparisons, we find that:

(1) The MB11 and HW06 models (bottom drag coefficient C_d= 0.005) yield virtually the same dynamic results;

(2) The observation-based momentum budgets (with C_d= 0.005-model local PGs and C_d=0.005) are considerably out-of-balance; because of the observed currents are considerably lower than the C_d= 0.005-model currents;
(3) The C_d= 0.01-model local PG and current amplitudes are significantly less than their C_d= 0.005-model counterparts;
(4) The observation-based momentum budgets (with C_d= 0.01-model local PGs C_d= 0.01) exhibit more balanced momentum budgets.

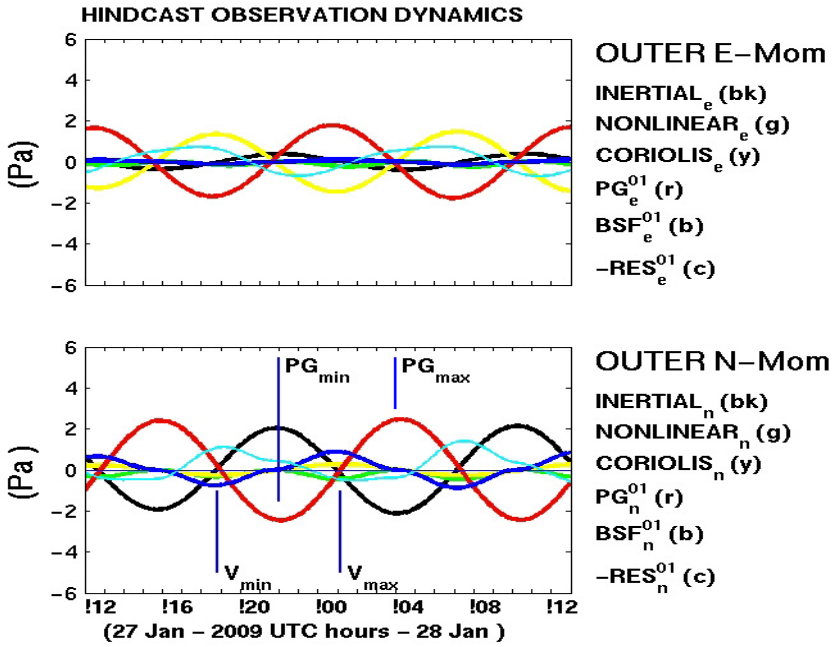

Figure 23 Observation-based *Outer Zone* momentum term estimates (in Pascals) for the (**upper**) E-W direction and (**lower**) N-S direction; with C_d = 0.01 and the model PGs for C_d = 0.01. The negative RES terms balance the momentum budget by definition. V and PG_yextrema times are indicated.

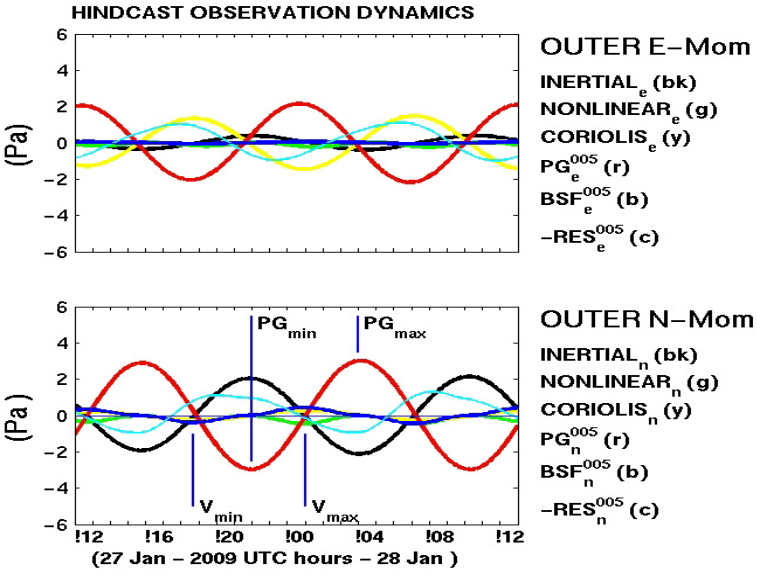

Figure 24Observation-based *Outer Zone* momentum term estimates (in Pascals) for the (**upper**) E-W direction and (**lower**) N-S direction; with $C_d = 0.005$ and the model PGs for $C_d = 0.005$. The negative RES terms balance the momentum budget by definition. V and PG extrema times are indicated.

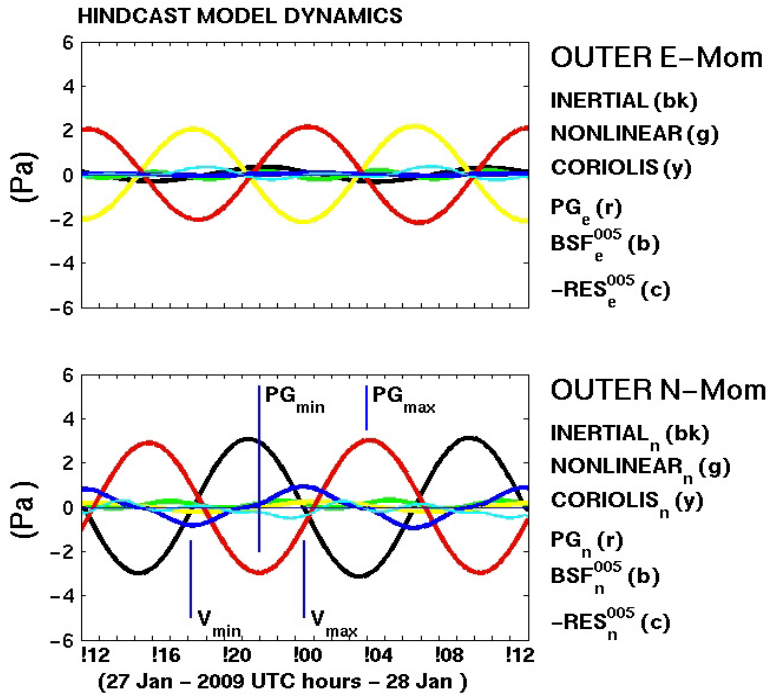

Figure 25 QUODDY **model-based** *Outer Zone* momentum term estimates (in Pascals) for the (**upper**) E-W direction and (**lower**) N-S direction; with $C_d = 0.005$ and the model PGs for $C_d = 0.005$. The negative RES terms balance the momentum budget by definition. V and PG_y extrema times are indicated.

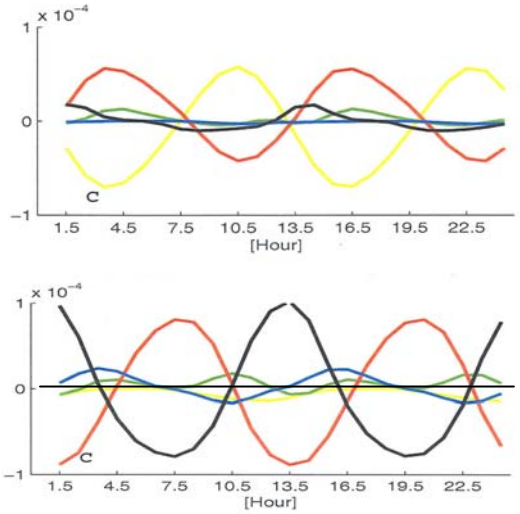

Figure 26 He and Wilkin (2006) **model-based** *Outer Zone* momentum term estimates (in m^2s^{-2}) for the (**upper**) E-W direction and (**lower**) N-S direction; with $C_d = 0.005$ at location C (see Figure 9). The momentum terms are inertial (bk); non-linear advection (g); Coriolis (y); pressure gradient (r); and bottom stress (bl) .

We conclude from these comparisons that the bottom stresses in our tidal eddy motion formation study region are larger than "normally-parameterized" bottom stresses; and using C_d= 0.01 produces relatively better momentum balances (i.e., dynamics) than C_d= 0.005 results. We carry these considerations forward as the vorticity dynamics of the study region are explored.

D. Eddy Motion Vorticity Dynamics

Given the basic rotary nature of the tidal eddy motion, we go on to consider it in a vorticity conservation framework. These GSC eddy motions are in some regards similar to the transient tidal eddies that Geyer and Signell (1990) investigated near Gay Head, Martha's Vineyard, MA. Thus we explore them in terms of the theoretical framework that is motivated by Signell and Geyer (1991).

The production, advection and dissipation of transient tidal motion can be viewed through the lens of the conservation of depth-averaged vorticity. Signell and Geyer (1991) present the balance between the *total change in vertical vorticity* ω following a fluid parcel and vorticity sources and sinks according to:

$$\frac{D\omega}{Dt} = A + B + C \qquad , \qquad (5)$$

where $\omega = \partial v/\partial x - \partial u/\partial y$, $\frac{D\omega}{Dt} = \frac{\partial \omega}{\partial t} + \vec{u} \bullet \nabla \omega$ in which $\vec{u}$ is the total velocity. The right-hand-side vorticity source/sink terms of Eq (5) (see Table 12) are A – due to friction-free water column stretching; B - due to frictional torque via three mechanisms; and C due to lateral vorticity diffusion via turbulent horizontal mixing.

The terms in Table 12 (except C – the vorticity diffusion) have been estimated for both the *Inner and Outer Zones* using the hindcast time series at TTE, NSA, NSD, and P as prescribed in the Appendix C algorithms. The vorticity budget is computed by adding the Eq(5) LHS terms to – (A+B) terms to produce a RESIDUAL; to which vorticity diffusion must contribute. (Note that the negative RESIDUAL term closes the budget by definition).

With reference to the slow CW transient tidal eddy motion formation period between 1800 and 2030 UTC, we note the negative (i.e., CW) vorticity is being produced in the *Inner Zone* because combined water column *stretching* and *slope torque* (+ RESIDUAL ~ *vorticity diffusion*) overcome the *positive vorticity* produced by the combined *speed torque* and *bottom frictional dissipation*;

At 2030 UTC, the net production of negative vorticity stops; coincident with the appearance of the model CW eddy motion (neg vorticity) near the coast;

Table 12 Depth-Averaged Vorticity Budget Terms: Estimation Methods, including CODAR (COD) and bottom pressure (BP) measurements. The variable definitions include where $\vec{u}$ is the total velocity**;** H = h + η is total water depth with mean water depth h and sea level departure η; C_D is the depth-averaged drag coefficient; and A_H is horizontal eddy viscosity – a parameterization of lateral turbulent mixing.

Eq(3) Term Definitions	Description	Variables
$A = \frac{\omega + f}{H}\left[\frac{\partial \eta}{\partial t} + \vec{u}\cdot\nabla H\right]$	**vorticity production** due to friction-free water column stretching; or squashing	f, ω, η, $\vec{u}$, H(x, y)
$B = -\left[\nabla \times \left(\frac{C_D \mid \vec{u} \mid \vec{u}}{H}\right)\right]\cdot\vec{k} = \mathrm{I} + \mathrm{II} + \mathrm{III}$	**vorticity production** due to bottom friction torque; in terms of three mechanisms	
$I = -\frac{C_D \mid \vec{u} \mid}{H^2}[\vec{u}\times\nabla H]\cdot\vec{k}$	**vorticity production** due to "slope torque"	C_D, $\vec{u}$, H(x, y)
$II = \frac{C_D(\vec{u}\times\nabla \mid \vec{u} \mid)\cdot\vec{k}}{H}$	**vorticity production** due to "speed torque"	C_D, $\vec{u}$, H(x, y)
$III = -\frac{C_D \mid \vec{u} \mid \omega}{H}$	**vorticity dissipation** due to bottom friction	C_D, $\vec{u}$, ω, H(x, y)
$C = A_H \nabla^2 \omega$	**vorticity diffusion** due to horizontal mixing	ω, A_H

The results indicate that the:

- I*nner zone* vorticity dynamics are much more energetic than the *outer zone* ones*;*
- I*nner zone* speed vorticity production is offset by the vorticity dissipation;
- Primary i*nner zone* balance is between the local vorticity rate change and the bottom frictional torque production;
- Speed vorticity production in the *outer zone* is balanced by a combination of local dissipation and the residual (probably vorticity diffusion out of the region).

6. Discussion

These findings beg a host of scientific questions concerning tide-related eddy motion in the western GoM, including: What are the size and energy ranges of this eddy motion? What are the mechanisms whereby the energetic tides of the region lead to the eddy motion generation and dissipation? How sensitive is the structure of this tidal eddy motion to the seasonally-changing stratification? How does the eddy motion modify the secondary flow environment of the dominant ebb and flood tidal flows that fill and empty the GoM? How are the dynamics of this transient eddy motion related to those of the tidal eddies reported by Geyer and Signell (1990) off of Gay Head/Martha's Vineyard, MA?

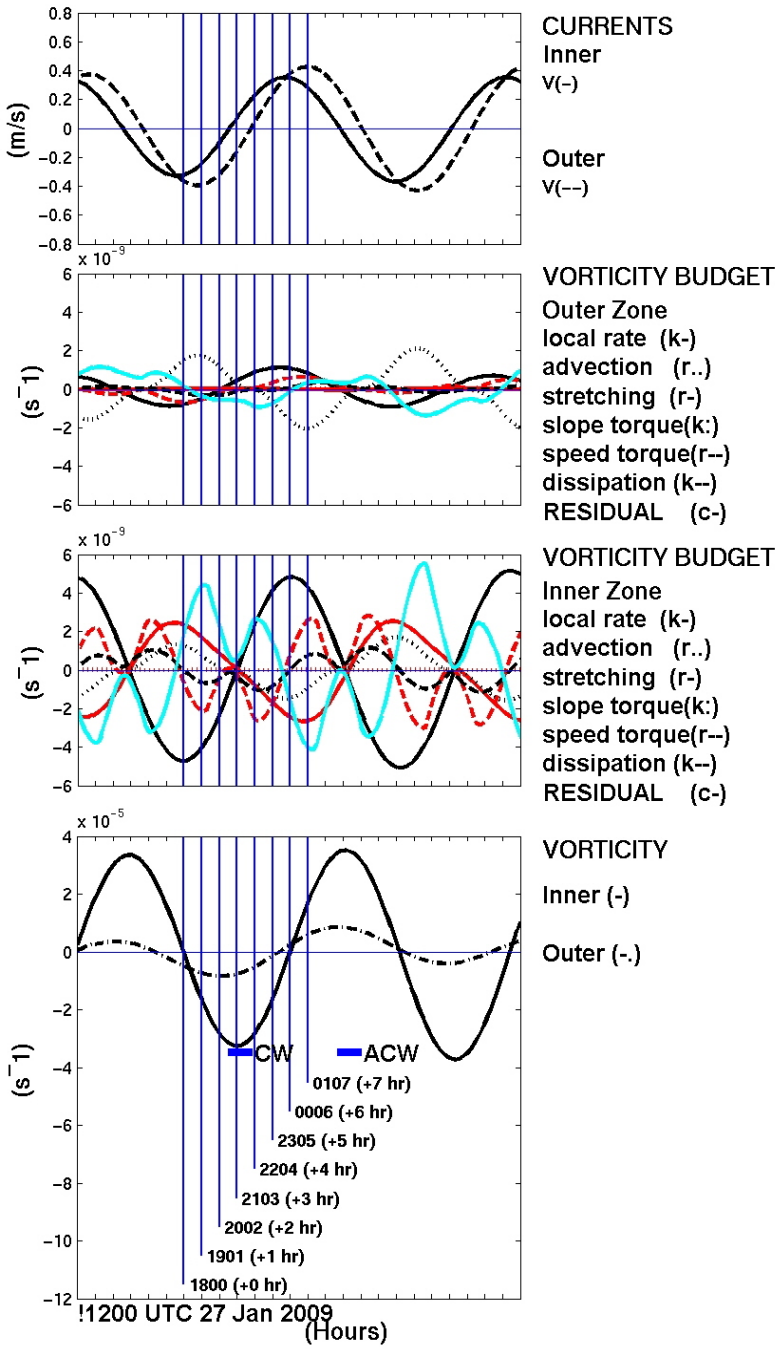

Figure 27 The *Inner* and *Outer Zone* **(top)** average V currents; **(bottom)** average vorticity with hourly milestone times; **(upper middle)** *Outer Zone* vorticity budget terms; **(lower middle)** *Inner Zone* vorticity budget terms including local time-rate change , advection , stretching production, friction torque production; speed torque production, dissipation via bottom friction ; and the negative RESIDUAL that closes the budget (by definition). The duration of the CW and ACW eddy motion in the study region is also indicated.

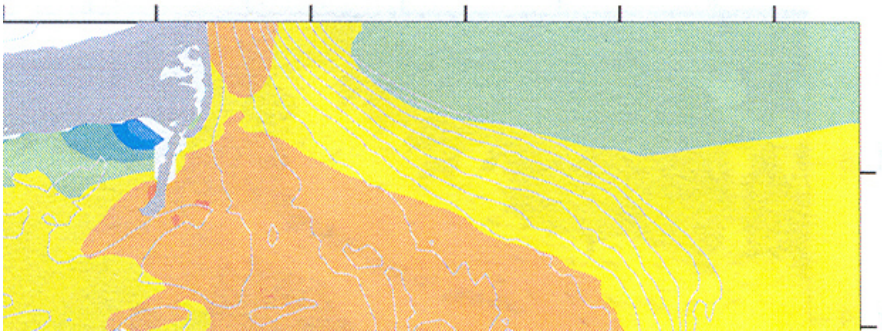

Figure 28 A zoom of the He and Wilkin (2006) model M_2 tidal energy dissipation distribution.

The price for the improved current comparison on the local study region was a significantly altered field of tidal characteristics throughout the rest of the GoM model domain. Thus, we conclude from this experiment that model bottom stress parameterization needs to be more spatially variable than is commonly employed in order to model this transient tidal eddy motion properly in our study region.

5. Summary of Conclusions

In early April 2005, a pair of high-frequency Coastal Ocean Dynamics Applications Radar (CODAR) stations on Cape Cod and Nantucket MA mapped clockwise (CW) and anticlockwise (ACW) eddy motion shortly after maximum ebb and flood tidal current respectively. These observations were validated by M_2 tide-forced, high-resolution, QUODDY finite-element numerical ocean model simulations of the formation of eddy motion near the coast off of Chatham, MA in our Great South Channel (GSC) study domain of the western Gulf of Maine. To better elucidate the kinematics and dynamics of these eddy motions, observational and model investigations were conducted during the very weakly stratified winter 2008-09 conditions.

The 5-constituent tidally-forced QUODDY model hindcast simulations mapped the formation, evolution and across-GSC translation of ebb flow-forced CW and flood flow-forced ACW eddy motions after the respective maximum flows. The field measurements, consisting of our moored bottom pressure (i.e., sea level) and ADCP current measurements at a nearshore site (TTE) in 13m depth, were augmented by 5-constituent tidal hindcasts of currents at several historical sites 10 to 30km to the east of TTE in water depths of ~33m. The dominant semidiurnal currents trace highly-rectified ellipses (~ 60km peak-to-peak) in the along-shore direction throughout the study region.

The observation-derived eddy motion kinematics are consistent with the model eddy motion center that propagated southeastward along curved 50m isobath at speeds that exceeded 5 m/s. The observation-based estimates of the momentum budget in the nearshore or Inner Zone (average depth ~20m) were dominated by the balance between the alongshore pressure gradient and bottom friction forces, with the inertial term being less important. With a relatively weaker bottom friction and stronger inertial term, all

three terms contributed more evenly to the offshore or Outer Zone (average depth ~30m) momentum budget.

The observation-based results, which employed a Cd = 0.01, were reasonably consistent with QUODDY model results with Cd = 0.01. However the QUODDY model results with Cd = 0.005 produced currents that were larger than the observations by about 50%. Thus we used Cd =0.01 in computing the observation-based estimates of the vorticity budget. The Inner Zone vorticity budget was dominated by a balance between the rate change of vorticity and the net of vorticity due to a sum of water column stretching-induced, slope torque-generated, plus offshore vorticity diffusion versus speed torque-induced plus bottom friction dissipation-induced vorticity.

The significant importance in bottom friction in these results led us to conclude that (1) a combination of strong alongshore pressure gradients and the bottom friction gradients in the shallower nearshore were responsible for generating the transient eddy motion and (2) its rapid offshore propagation speed of both the CW and ACW phase eddies are the dynamic signatures of the change of tide in the GSC.

6. Appendices

APPENDIX A: Observed and Model Current and Bottom Pressure Tides

Our station TTE measurements and tidal hindcasts based on historical measurements (see Moody et al., 1984) at an array of sites (located in Table A1 and main text Figures 2, 8, and 9) were used for our analysis. The station TTE moored ADCP current time series at 6m and 8m elevations above bottom (AB) off of Chatham, MA were interpolated to an even 10-minute intervals starting at 0000 GMT 4 November 2008 [954096.00 Julian hours (JH) - referenced to 0000 GMT 1 January 1900] and ending at 0000 GMT 30 December 2008 (955440 JH). (The basic statistics including variance ellipse characteristics of these 57-day series are given in Table 2 - main text).

Table A1 Station locations for bottom pressure and current measurements at TTE and a suite of historical stations for which we have tidal harmonic constants (see Moody et al., 1984) based on measurements, including ones off of Nauset, MA (NAU) and the north flank of Georges Bank (M1),. Record depths and lengths are provided.

Station ID	Location		Sensor	Series
	Long. °W	Lat. °N	Depth (m)	Length (Days)
Bottom Pressure				
TTE	69. 923	41.658	13	58
NAU	69.933	41.817	7	58
M1	67.867	42.067	179	556
Current				
TTE	69. 923	41.658	5,7	58
NSA	69.600	41.520	5, 25	60
NSB	69.730	41.430	10	42
NSD	69.730	41.620	16	42

The harmonic analysis results for the array of bottom pressure series (Table A2) show that the regional tidal sea level variability clearly dominated by the M_2 semidiurnal tides.

Table A2a The *observed* bottom pressure (BP) tidal harmonic constants (amplitudes in decibars and Greenwich epoch phases) of the principal plus 2 nonlinear tidal constituents based on an analysis of the 57-day record (3 November to 30 December 2008) at station TTE. These are compared the Moody et al. (1984) harmonic constants for the historical BP measurements at stations off of Nauset, MA (NAU), the north flank of Georges Bank (M1). Typical analysis uncertainties are given.

Con	TTE Amp (db)	TTE Phase (G^o)	NAU Amp (db)	NAU Phase (G^o)	M1 Amp (db)	M1 Phase (G^o)
M_2	**1.103 ±0.013**	**119 ± 1**	**1.032**	**102**	**0.782**	**92**
N_2	0.238 ±0.013	96 ± 3	0.222	70	0.180	63
S_2	0.170 ±0. 013	156 ± 4	0.144	133	0.122	121
K_1	0.132 ±0. 013	192 ± 6	0.131	201	0.112	199
O_1	0.114 ±0. 013	209 ± 5	0.115	182	0.085	185
M_4	0.027	16	-	-	-	-
M_6	0.030	178	-	-	-	-

The harmonic analysis results of the station TTE current series (Table A3) also show that they are clearly dominated by the M_2 semidiurnal tidal variability. Not surprisingly, the M_2 tidal current ellipse for near-shore tidal flow is nearly rectilinear in the direction of the bathymetry. The M_2 tidal current ellipse characteristics of the historical moored current measurements (located in Figure A1; Table A1) in Table A4 are consistent with those at TTE in prompting us to align the analysis coordinate system with the tides (X-120^{o}T; Y-30^{o}T).

Table A2b The *model* bottom pressure record harmonic constants (amplitudes in decibars and Greenwich epoch phases) of the principal plus 2 nonlinear tidal constituents based on the 30-day simulation records. Typical analysis uncertainties are given.

Con	TTE Amp (db)	TTE Phase (G^o)	NAU Amp (db)	NAU Phase (G^o)	M1 Amp (db)	M1 Phase (G^o)	TTE' Amp (db)	TTE' Phase (G^o)
M_2	**1.101 ±0.009**	**123 ±1**	**1.109**	**118**	**0.859**	**93**	**1.061**	**124**
N_2	0.179 ±0.009	90 ± 3	0.182	85	0.148	61	0.174	91
S_2	0.154 ±0.009	168 ± 4	0.158	162	0.130	136	0.149	169
K_1	0.075 ±0.009	215 ± 6	0.074	215	0.063	204	0.075	190
O_1	0.076 ±0.009	190 ± 5	0.076	190	0.069	189	0.076	216
M_4	0.061	25	0.067	12	0.028	26	0.057	25
M_6	0.010	3	0.007	336	0.016	299	0.010	12

Table A2c The harmonic constants for the principal plus non-linear tidal constituents of the *model local* northward bottom pressure gradient based on the 30-day simulation record (3 November to 4 December 2008) at the indicated stations. Typical analysis uncertainties are given.

Con	NAU Amp (10^5 x db/m)	NAU Phase (G^o)	TTE Amp (10^5 x db/m)	TTE Phase (G^o)	TTE' Amp (10^5 x db/m)	TTE' Phase (G^o)	NSD Amp (10^5 x db/m)	NSD Phase (G^o)	NSA Amp (10^5 x db/m)	NSA Phase (G^o)
M_2	**0.448**	**49**	**1.063 ±0.003**	**59 ± 0**	**1.100**	**69**	**0.867**	**64**	**1.036**	**88**
N_2	0.069	21	0.158 ±0.003	34 ± 1	0.163	44	0.131	34	0.161	59

S_2	0.065	102	0.154 ±0.003	114 ± 1	0.160	124	0.124	115	0.154	139
K_1	0.005	89	0.009 ±0.003	118 ± 19	0.009	150	0.011	99	0.017	155
O_1	0.002	133	0.007 ±0.003	146 ± 22	0.011	148	0.004	111	0.009	151
M_4	0.044	324	0.174	322	0.171	328	0.089	334	0.100	346
M_6	0.023	178	0.046	268	0.048	294	0.034	282	0.028	3

Table A2d The harmonic constants for the principal plus non-linear tidal constituents of the TTE-NAU estimates of the *model* (MOD) and *observed* (OBS) *large-scale* northward pressure gradient force (PGF_n). Typical analysis uncertainties are given.

Con	**MOD PGF_n Amp** (10^5 x db/m)	**MOD PGF_n Phase** (G^o)	**OBS PGF_n Amp** (10^5 x db/m)	**OBS PGF_n Phase** (G^o)
M_2	**0.576 ±0.002**	**35 ±0**	**1.894 ±0.08**	**8 ±2**
N_2	0.082±0.002	15 ± 1	0.586±0.08	331 ± 7
S_2	0.083 ±0.002	89 ± 1	0.058 ±0.06	23 ± 67
K_1	0.006 ±0.002	68 ± 19	0.149 ±0.08	349 ± 102
O_1	0.000 ±0.002	89 ± 22	0.089 ±0.07	110 ± 30
M_4	0.088	308	0.157	195
M_6	0.029	223	0.169	1

Table A3 The tidal harmonic constants for the five principal and 2 nonlinear constituents of the moored station TTE eastward and northward currents at 6m and 8m AB between 3 November and 29 December 2008 (56 days) in terms of component amplitude and Greenwich epoch phases. The tidal current ellipses are given in terms of major axis amplitude and orientation, ellipticity (ε=major/minor), with a positive major axis amplitude indicating an anti-clockwise rotating current vector; and the Greenwich phase of the maximum current.

Tidal Const	**Total Var** $(cm/s)^2$	**East Amp** (cm/s)	**Phase** (G^o)	**North Amp** (cm/s)	**Phase** (G^o)	**Major Axis Amp** (cm/s)	**Maj Axis Dir** (^oT)	**ε**	**V_{max}** (G^o)
6m									
M_2	**1960**	**21.2 ±0.5**	**272 ± 1**	**38.8 ±1.1**	**275 ± 1**	**44.3**	**29**	**37**	**274**
N_2	62	3.7 ±0.5	244 ± 7	6.7 ±1.1	252 ± 9	7.7	29	19	250
S_2	61	2.1 ±0.5	312 ±12	6.4 ±1.1	313 ± 7	6.7	18	∞	313
K_1	3	0.9 ±0.5	302 ±35	1.5 ±1.1	260 ±39	1.6	25	-3	270
O_1	0	0.24±0.4	324 ±75	0.1 ±0.1	241±106	0.4	88	∞	324
M_4	6	1.1	146	2.3	116	2.6	21	4	170
M_6	1	0.8	16	0.8	296	1.1	56	11	21
8m									
M_2	**2185**	**23.0 ±0.5**	**272 ± 1**	**40.7 ±1.1**	**275 ± 1**	**46.7**	**30**	**42**	**274**
N_2	67	3.9 ±0.5	244 ± 7	7.0 ±1.1	252 ± 9	8.0	29	16	251
S_2	65	2.1 ±0.5	312 ±12	6.7 ±1.1	312 ± 7	7.0	17	∞	313
K_1	3	0.9 ±0.5	296 ±35	1.7 ±1.1	260 ±39	1.9	25	-4	268
O_1	0	0.2 ±0.4	335 ±75	0.1 ±0.1	129±106	0.2	282	∞	334
M_4	5	1.0	139	2.2	116	2.3	21	4	170
M_6	1	0.9	18	0.6	296	1.1	56	11	21

Table A4 The M_2 constituent harmonic constants for the 3 November and 27 December 2008 (56 days) measurements at station TTE as well as the Moody et al., (1984) 5-constituent hindcast current series at stations NSA, NSB, NSD, NSB-NSD interpolated P, NSC, and NSE. Current component harmonic amplitudes and phases in Greenwich epoch are given; along with the tidal current constituent ellipses in terms of major axis amplitude and orientation, ellipticity (ε=major/minor) - with a positive major axis amplitude indicating an anti-clockwise rotating current vector, and Greenwich phase of the maximum current.

Tidal Cons	**Sensor Depth** (m)	**East Amp** (cm/s)	**East Ph** (^oG)	**North Amp** (cm/s)	**North Ph** (^oG)	**Major Amp** (cm/s)	**Major Dir** (^oT)	**ε**	**Vmax Ph** (^oG)
TTE	6	21	272	39	275	44	29	37	274
TTE	8	23	272	41	275	47	30	43	274
TTE	**AVE**	**22**	**272**	**40**	**275**	**46**	**29**	**38**	**274**
NSA	5	6	40	59	345	59	4	-9	345
NSA	25	6	16	59	319	59	3	-11	320
NSA	**AVE**	**7**	**28**	**58**	**331**	**58**	**4**	**-10**	**331**
NSB	**10**	**37**	**20**	**63**	**345**	**71**	**28**	**-4**	**353**
NSD	**16**	**21**	**327**	**41**	**345**	**46**	**27**	**8**	**342**
P	**NA**	**9**	**273**	**40**	**303**	**41**	**11**	**9**	**302**
NSC	8	46	32	15	247	47	285	-6	35
NSE	10	39	10	35	266	41	301	-1	35

Table A5 The M_2 constituent harmonic constants for the depth-averaged *rotated currents* for our TTE and the Moody et al. (1984) station NSA. Harmonic constants for the NSB 10m, NSD 16m currents are also presented (see Appendix A; Tables A-3; A-4). The "station P" harmonic constants were derived from the a weighted average of Station D and Station D hindcast tidal currents The component amplitudes and phases (in Greenwich epoch) are given along with the tidal current ellipse in terms of major axis amplitude and orientation, ellipticity (ε=major/minor) - with a positive major axis amplitude indicating an anti-clockwise rotating current vector, and Greenwich phase of the maximum current.

Tidal Cons	**Sta Depth** (m)	**U Amp** (cm/s)	**U Ph** (°G)	**V Amp** (cm/s)	**V Ph** (°G)	**Major Amp** (cm/s)	**Major Dir** (°T)	**ε**	**Max Ph** (°G)
TTE Ave	13	1	155	46	274	46	29	41	274
NSA Ave	33	26	139	52	334	58	4	- 10	331
NSD 16m	33	6	226	46	341	46	27	8	341
NSB 10m	23	19	91	71	354	71	28	- 4	353
P	30	4	164	52	345	52	26	517	345

Table A6 The M_2 constituent harmonic constants for the "observed " and modeled "depth-averaged" current components at TTE, NSA, and NSD; based on a harmonic analysis of for 30 days starting at 0000 GMT 4 November 2008 (also see Appendix A; Tables A3; A4). The component harmonic amplitudes and phases in Greenwich epoch are given; along with the tidal current constituent ellipses in terms of major axis amplitude and orientation, ellipticity (ε=major/minor) - with a positive major axis amplitude indicating an anti-clockwise rotating current vector, and Greenwich phase of the maximum current.

Tidal Cons	**East Amp** (cm/s)	**East Ph** (°G)	**North Amp** (cm/s)	**North Ph** (°G)	**Major Amp** (cm/s)	**Major Dir** (°T)	**ε**	**Vmax Ph** (°G)
TTE	**24**	**272**	**41**	**276**	**47**	**30**	**36**	**275**
Model	25	316	64	300	68	21	-11	302
NSA	**7**	**28**	**57**	**330**	**57**	**4**	**-10**	**331**
Model	12	34	75	338	75	5	-13	339
NSD	**21**	**327**	**41**	**345**	**46**	**27**	**8**	**341**
Model	8	293	55	321	56	7	15	321

APPENDIX B: Comparison of Observed and Model Dynamics

The momentum and vorticity budgets are estimated using the algorithms and approximations described below for the *Inner and Outer Zones* in the rotated (30° clockwise) coordinate system; as defined in main text (see Figure 9). The basis for this analysis is as follows.

The vector form of the momentum equations is

$$\frac{D\vec{u}}{Dt} = \frac{\partial \vec{u}}{\partial t} + \vec{u} \bullet \nabla \vec{u} - \vec{f} x \vec{u} = -\frac{1}{\rho}\nabla p + \frac{1}{\rho}\left[\nabla \bullet \vec{\vec{\sigma}}\right] \quad , \qquad \text{(B1)}$$

where $\vec{u} = u\vec{i} + v\vec{j} + w\vec{k}$ is the total velocity; f is the Coriolis parameter, ρ = water density, p is pressure, and $\vec{\vec{\sigma}}$ is the stress tensor.

The component-form of the momentum equations (Eq. B1) were vertically-integrated and area-averaged over our study region following the Brown (1984) application to external

tidal variability on Georges Bank. Assuming negligible stratification effects, the different volume-averaged terms in the

x-direction are

$$\frac{\rho_o}{A}\left\{\frac{\delta[u]}{\delta t}+\left\langle\delta_x\overline{uu}\right\rangle_y+\left\langle\delta_y\overline{uv}\right\rangle_x-f[v]+\frac{1}{\rho_o}\left\langle h\frac{\partial p_b}{\partial x}\right\rangle-\frac{1}{\rho_o}\left\langle\tau_x^s-\tau_x^b\right\rangle-\frac{1}{\rho_o}\left\langle\frac{\partial hT_x}{\partial x}+\frac{\partial hT_x}{\partial y}\right\rangle\right\}=0\ ; \qquad \text{(B2a)}$$

y-direction are

$$\frac{\rho_o}{A}\left\{\frac{\delta[v]}{\delta t}+\left\langle\delta_x\overline{uv}\right\rangle_y+\left\langle\delta_y\overline{vv}\right\rangle_x+f[u]+\frac{1}{\rho_o}\left\langle h\frac{\partial p_b}{\partial y}\right\rangle-\frac{1}{\rho_o}\left\langle\tau_y^s-\tau_y^b\right\rangle-\frac{1}{\rho_o}\left\langle\frac{\partial hT_y}{\partial x}+\frac{\partial hT_y}{\partial y}\right\rangle\right\}=0\,, \qquad \text{(B2b)}$$

inertial — nonlinear — Coriolis — pressure gradient — horizontal stress — lateral stress

where the domain area $A=\Delta x\Delta y=(x_2-x_1)(y_2-y_1))$, ρ_o is the reference water density, p_b is bottom pressure, τ^s is surface stress, τ^b is bottom stress, and the notation for the different integrals and differences are:

$$\overline{.....}\equiv\int_{-h}^{\eta}.....dz\ ;\ [.....]\equiv\int_{y1}^{y2}\int_{x1}^{x2}\int_{-h}^{\eta}.....dxdydz\ ;\ \langle....\rangle\equiv\int_{y1}^{y2}\int_{x1}^{x2}.....dxdy\ ;$$

$$\langle....\rangle_y\equiv\int_{y1}^{y2}.....dy\ ;\ \langle....\rangle_x\equiv\int_{x1}^{x2}.....dx$$

$\delta_x f(x,y)=f(x_2)-f(x_1)$, and $\delta_y f(x,y)=f(y_2)-f(y_1)$.

For this study, (1) surface stress τ^s was assumed zero and (2) the lateral gradient of the Y-directed lateral stress component $\left\langle\frac{\partial hT_y}{\partial x}\right\rangle=\left\langle\delta_x hT_y\right\rangle_y$, while smaller than the bottom stress, was retained. Thus Eq (B2) becomes for the

X-direction:

$$\frac{\rho_o}{A}\left\{\frac{\delta[u]}{\delta t}+\left\langle\delta_x\overline{uu}\right\rangle_y+\left\langle\delta_y\overline{uv}\right\rangle_x-f[v]+\frac{1}{\rho_o}\left\langle h\frac{\partial p_b}{\partial x}\right\rangle+\frac{1}{\rho_o}\left\langle\tau_x^b\right\rangle\right\}=RES_x \qquad \text{(B3a)}$$

and Y-direction:

$$\frac{\rho_o}{A}\left\{\frac{\delta[v]}{\delta t}+\left\langle\delta_x\overline{uv}\right\rangle_y+\left\langle\delta_y\overline{vv}\right\rangle_x+f[u]+\frac{1}{\rho_o}\left\langle h\frac{\partial p_b}{\partial y}\right\rangle+\frac{1}{\rho_o}\left\langle\tau_y^b\right\rangle-\frac{1}{\rho_o}\left\langle\delta_x hT_y\right\rangle_y\right\}=RES_y\,, \qquad \text{(B3b)}$$

inertial — A nonlinear B — Coriolis — pressure gradient — horiz stress — lateral stress

where the residual (RES) components are the sum of neglected terms and the errors in estimating the terms on the left-hand-side of the equations.

We estimated the bottom stress component terms at each station by using estimates of the local bottom currents and the same quadratic bottom stress law used in the

model. For example, the nonlinear x-directed bottom stress component at station TTE was computed according to

$$\tau_x^b = \rho_o C_d \left(\sqrt{\left(u_{TE}^{bot}\right)^2 + \overline{\left(v_{TE}^{bot}\right)^2}} \right) u_{TE}^{bot} \quad , \qquad \text{(B4a)}$$

where C_d is the bottom drag coefficient and u_{TE}^{bot} is a bottom current (at Station TTE in this case). On the basis of an inspection of the model current profiles, bottom currents at each station were estimated as 0.60 x local depth-averaged currents. The spatially-averaged x-directed bottom stresses for the *Inner Zone (IZ)* was estimated by simple averaging of the Eq (B4a) bottom stress estimates at stations TTE and P according to:

$$\frac{1}{A}\left\langle \tau_x^b \right\rangle \approx \frac{\rho_o C_D}{2}\left[\left| \sqrt{\left(\overline{u_{TE}}\right)^2 + \left(\overline{v_{TE}}\right)^2} \right| \left(\overline{u_{TE}}\right) + \left| \sqrt{\left(\overline{u_P}\right)^2 + \left(\overline{v_P}\right)^2} \right| \left(\overline{u_P}\right) \right]. \qquad \text{(B4b)}$$

Stations NSA and NSD currents were used to compute the *Outer Zone* (*OZ*) bottom stress.

The most significant lateral stress term (see Eq B3b) was estimated at each station in terms of the parameterized vertically-averaged lateral stress given by

$$T_y = \rho_o L_D \left[\left(\overline{v}\right)^2 / h^{\,2} \right], \qquad \text{(B5a)}$$

where L_D is the lateral "drag coefficient", which was assumed to be 1 in this case. The algorithms used to compute the zone–averaged lateral stress are given in Appendix B. for the *Inner* and *Outer Zones* according to the following:

$$\frac{1}{A}\left\langle \delta_x h T_y \right\rangle_y \approx \frac{1}{A}\left(h_P T_y^{\,P} + h_{TE} T_y^{\,TE} \right) \Delta y \approx \frac{\rho_o L_D}{\Delta x}\left[\left(\overline{v_P}\right)^2 / h_P + \left(\overline{v_{TE}}\right)^2 / h_{TE} \right], \qquad \text{(B5b)}$$

$$\frac{1}{A}\left\langle \delta_y h T_x \right\rangle_x \approx \frac{1}{A}\left(h_P T_x^{\,D} + h_{TE} T_x^{\,TP} \right) \Delta x \approx \frac{\rho_o L_D}{\Delta y}\left[\left(\overline{u_D}\right)^2 / h_D + \left(\overline{u_P}\right)^2 / h_P \right], \qquad \text{(B5c)}$$

$$\frac{1}{A}\left\langle \delta_x h T_y \right\rangle_y \approx \frac{1}{A}\left(h_A T_y^{\,A} + h_D T_y^{\,D} \right) \Delta y \approx \frac{\rho_o L_D}{\Delta x}\left[\left(\overline{v_A}\right)^2 / h_A + \left(\overline{v_D}\right)^2 / h_D \right], \qquad \text{(B5d)}$$

where Eqs (B5b) and (B5c) pertain to the *IZ* and Eqs (B5c) and (B5d) pertain to the *OZ*.

The time series of these terms were estimated using algorithms detailed below and the 5-tidal constituent hindcasts of observed currents at stations detailed in Table B1a (also Figure 9) and Table B1b (also Figure 2). The corresponding model current and pressure station locations and separations are detailed in Tables B2a and b.

Table B1a The locations of the OBSERVED *current stations* (including historical stations; Moody et al., 1984) with water and sensor depths. The matrix shows station separation distances and bearings (°T), inverse separation distances (…) in units $10^5 m^{-1}$ and record lengths RL used to obtain harmonic constants.

ID	Location		Depths							
	Lat. (°N)	**Long.** (°W)	water (senAB) (m)	RL (da)	TTE (km) (°T)	NSD (km) (°T)	P (km) (°T)	NSB (km) (°T)	NSA (km) (°T)	Outer (km) (°T)
TTE	41°39'13"	69° 55'28"	13	58	-	16.59 (6.028)	15.52 (6.443)	30.01 (3.332)	30.94 (3.232)	
	41.658	69. 923	(5/7)		-	105	119	147	119	
NSD	41° 37'	69° 44'	33	42	16.59 (6.028)	-	4.17 (23.98)	21.13 (4.710)	15.51 (6.448)	
	41.620	69.730	(16)		105	-	36	180	136	
P	41°34'52"	69°44	30	NA	15.52 (6.443)	4.17 (23.98)	-	17.97 (5.565)	15.47 (6.464)	
	41.590	69.730			299	36	-	172	119	
NSB	41° 26'	69° 44'	22	42	30.01 (3.332)	21.13 (4.710)	17.97 (5.565)	-	14.7 (6.803)	
	41.430	69.730	(10)		327	0	352	-	47	
NSA	41° 31'	69° 36'	33	60	30.94 (3.232)	15.51 (6.448)	15.47 (6.464)	14.7 (6.803)	-	
	41.520	69.600	(5/25)		119	136	2.99	227	-	
Inner	41.639	69.827	23	NA						15.5 (6.452)
										119
Outer	41.570	69.665	33	NA						

Table B1b The locations of the OBSERVED *bottom pressure stations* (including historical stations; Moody et al., 1984) with water and sensor depths. The matrix shows station separation distances and bearings (°T). Inverse separation distances (…) in units of $10^5 m^{-1}$ and time series record lengths (RL) are also included.

ID	Location		Depth				
	Lat. (°N)	**Long.** (°W)	water (senAB) (m)	RL (days)	M1 (km) (°T)	NAU (km) (°T)	TTE (km) (°T)
M1	42° 04'	67° 52'	184	556	-	173.0 (0.578)	176.2 (0.568)
	42.067	67. 867	(5)		-	260	254
Mid –NAU/M1	41.942	68.900					
NAU	41° 49'	69° 23'	7	58	173.0	-	17.7 (5.650)
	41.817	69.933	(1)		80	-	177
Mid-TTE/NAU	41.738	69.928					
TTE	41°39'13"	69° 55'28"	13	58	176.2	17.7	-
	41.658	69. 923	(1)		74	177	-

Table B2a The locations of the MODEL current and local pressure gradient stations with corresponding model water depths; as well as the *Inner* and *Outer Zones*. The matrix shows station separation distances and bearings (°T). Inverse separation distances (…) in units of $10^5 m^{-1}$.

	Lat. (°N)	**Long.** (°W)	**Dep** (m)	NTE (km) (°T)	TTE' (km) (°T)	NSD (km) (°T)	P (km) (°T)	NSB (km) (°T)	NSA (km) (°T)	Outer (km) (°T)
NTE	41.67	69. 93	15	-	6.7 (14.925)	17.0 (5.882)	18.9 (5.291)	31.4 (3.185)	32.3 (3.096)	
				-	132	101	118	148	119	
TTE'	41.63	69. 87	21	6.7 (14.925)	-	11.7 (8.547)	12.5 (8.000)	26.4 (3.788)	25.8 (3.876)	
				132	-	84	110	147	115	
NSD	41.64	69.73	33	17.0 (5.882)	11.7 (8.547)	-	5.6 (17.86)	23.5 (4.255)	16.9 (5.917)	
				101	264	-	179	173	136	
P	41.59	69.73	30	18.9 (5.291)	12.5 (8.000)	5.6	-	18.0 (5.555)	13.4 (7.462)	
				118	290	359	-	171	119	
NSB	41.43	69.73	22	31.4 (3.185)	26.4 (3.788)	23.5 (4.255)	18.0 (5.555)	-	14.4 (6.944)	
				148	327	153	351	-	39	
NSA	41.53	69.59	40	32.3 (3.096)	25.8 (3.876)	16.9 (5.917)	13.4 (7.463)	14.4 (6.944)	-	
				119	295	316	299	219	-	
Inner	*41.639*	*69.827*	*23*							*15.5 (6.452)*
Outer	*41.570*	*69.665*	*33*							*119*

Table B2b The locations of the MODEL *pressure stations* with model water depths and station separation distances and bearings (°T). Inverse separation distances (…) are in units of 10^5 m^{-1}.

ID	**Location**		**Depth**			
	Lat. (°N)	**Long.** (°W)	water (m)	M1 (km) (°T)	NAU (km) (°T)	TTE (km) (°T)
M1	42.07	67. 87	180	-	170.0 (0.588)	176.0 (0.568)
				-	259	254
Mid –NAU/M1	41.94	68.88				
NAU	41.80	69.89	7	170.0	-	14.8 (6.757)
				79	-	192
Mid-TTE/NAU	41.74	69.91				
TTE	41.67	69. 93	15	176.0	14.8	-
				74	177	-

The Eq (B2) volume-integrated momentum term time series were estimated using the both the observation-based algorithms (Table B3) and the model-based algorithms (Table B4) and the relevant 5-constituent tidal harmonic hindcast time series from both the *Inner and Outer Zones* respectively. (NOTE: We verified that the phase differences between

momentum terms estimated, using either the 5-tidal constituent series, and those using the M_2-only tidal series were small).

Table B3a The algorithms for estimating the pressure gradient terms in the volume-integrated momentum equations (Eq E2) using the indicated *Inner and Outer Zone* model local pressure gradient hindcast time series (Figure 9 stations IDs). *T*he assumptions are given for each algorithm, which employ parameter values: $\Delta x = 15.47$ km; $\Delta y = 4.17$ km; $h_{TE} = 13$m $h_P = 30$m; $h_D = 33$m; and $h_A = 33$m.

Site	Term	Estimate Algorithm	Assumptions
Inner			
	$\frac{\partial p_b}{\partial EW}$	$\frac{\left[\frac{\partial p_{bTTE}}{\partial EW}(dbar/m)+\frac{\partial p_{bP}}{\partial EW}(dbar/m)\right]}{2}$	$\frac{10^{4}}{\Delta_{NAU-M1}} = 5.78x10^{-2}\frac{(kg/s^2m^2)}{dbar}$
	$\frac{\partial p_b}{\partial NS}$	$\frac{\left[\frac{\partial p_{bTTE}}{\partial NS}(dbar/m)+\frac{\partial p_{bP}}{\partial NS}(dbar/m)\right]}{2}$	$\frac{10^{4}}{\Delta_{NAU-TTE}} = 56.50x10^{-2}\frac{(kg/s^2m^2)}{dbar}$
	$\frac{\rho_o}{A}\left(\frac{1}{\rho_o}\langle h\partial p_b/\partial x\rangle\right)$	$[(h_{TE}+h_P)0.5]\bullet CWrot30^o\left(\frac{\partial p_b}{\partial EW}\right)$	$(h_{TTE}+h_P)0.5 = 21m$ (constant on A)
	$\frac{\rho_o}{A}\left(\frac{1}{\rho_o}\langle h\partial p_b/\partial y\rangle\right)$	$[(h_D+h_P)0.5]\bullet CWrot30^o\left(\frac{\partial p_b}{\partial NS}\right)$	$(h_D+h_P)0.5 = 32m$ (constant on A)
Outer	$\frac{\rho_o}{A}\left(\frac{1}{\rho_o}\langle h\partial p_b/\partial x\rangle\right)$	$[(h_A+h_D)0.5]\bullet CWrot30^o\left(\frac{\partial p_b}{\partial EW}\right)$	$(h_D+h_A)0.5 = 33m$ (constant on A)
	$\frac{\rho_o}{A}\left(\frac{1}{\rho_o}\langle h\partial p_b/\partial y\rangle\right)$	$[(h_D+h_P)0.5]\bullet CWrot30^o\left(\frac{\partial p_b}{\partial NS}\right)$	$(h_D+h_P)0.5 = 32m$ (constant on A)

Table B3b OBSERVED *Inner Zone* ESTIMATES: A summary of the approximations and corresponding assumptions used to estimate the *rotated velocity-related terms* (units Pa = N/m^2) in the volume-integrated momentum equations according to Eq (B2); using *observed* hindcast series with subscripts referenced to the stations IDs in Figure 9; with Δx = 15.47 km; Δy = 4.17 km; h_{TE}= 13m h_P= 30m; and h_D = 33m.

Data	Term	Estimate Algorithm	Assumptions
Inner	$[u]$	$\left\{\left(\overline{u_P}\right)0.5+0.5\overline{u_{TE}}\right\}(\Delta x\Delta y)$	linear velocity variation
	$[v]$	$\left\{\left(\overline{v_P}\right)0.5+0.5\overline{v_{TE}}\right\}(\Delta x\Delta y)$	linear velocity variation
Inertial_x	$\frac{\rho_o}{A}\frac{\delta[u]}{\delta t}$	$(1025.7)\frac{\delta}{\delta t}\left\{\left(\overline{u_P}\right)0.5+0.5\overline{u_{TE}}\right\}$	$\rho_o = 1025.7\,kg/m^3$
Inertial_y	$\frac{\rho_o}{A}\frac{\delta[v]}{\delta t}$	$(1025.7)\frac{\delta}{\delta t}\left\{\left(\overline{v_P}\right)0.5+0.5\overline{v_{TE}}\right\}$	$\rho_o = 1025.7\,kg/m^3$
Coriolis_x	$-\frac{\rho_o f}{A}[v]$	$-(0.09905)\frac{\delta}{\delta t}\left\{\left(\overline{v_P}\right)0.5+0.5\overline{v_{TE}}\right\}$	$\rho_o f = 0099\,kg/s\cdot m^3$
Coriolis_y	$+\frac{\rho_o f}{A}[u]$	$(0.09905)\frac{\delta}{\delta t}\left\{\left(\overline{u_P}\right)0.5+0.5\overline{u_{TE}}\right\}$	$\rho_o f = 0099\,kg/s\cdot m^3$
NonLinA_x	$\frac{\rho_o}{A}\left\langle\delta_x\overline{uu}\right\rangle_y$	$\frac{\rho_o}{\Delta x}\left[\left(\overline{u_P u_P}/h_P\right)-\left(\overline{u_{TE}u_{TE}}/h_{TE}\right)\right]$	no y-var of $\delta_x\overline{uu}$ $\frac{\rho_o}{\Delta x h_{TE}} = 5.10x10^{-3}\frac{kg}{m^5}$ $\frac{\rho_o}{\Delta x h_P} = 2.21x10^{-3}\frac{kg}{m^5}$
NonLinB_x	$\frac{\rho_o}{A}\left\langle\delta_y\overline{uv}\right\rangle_x$	$\frac{\rho_o}{\Delta y}\left[\left(\overline{u_D v_D}/h_D\right)-\left(\overline{u_P v_P}/h_P\right)\right]$	no x-var of $\delta_y\overline{uv}$ $\frac{\rho_o}{\Delta y h_D} = 7.45x10^{-3}\frac{kg}{m^5}$ $\frac{\rho_o}{\Delta y h_P} = 8.2x10^{-3}\frac{kg}{m^5}$
NonLinA_y	$\frac{\rho_o}{A}\left\langle\delta_x\overline{uv}\right\rangle_y$	$\frac{\rho_o}{\Delta x}\left[\left(\overline{u_P v_P}/h_P\right)-\left(\overline{u_{TE}v_{TE}}/h_{TE}\right)\right]$	no y-var of $\delta_x\overline{uv}$
NonLinB_y	$\frac{\rho_o}{A}\left\langle\delta_y\overline{vv}\right\rangle_x$	$\frac{\rho_o}{\Delta y}\left[\left(\overline{v_D v_D}/h_D\right)-\left(\overline{v_P v_P}/h_P\right)\right]$	no x-var of $\delta_y\overline{vv}$
$\underline{\text{BotStress}_x}$	$\left(\frac{1}{A}\left\langle\tau_x^b\right\rangle\right)$	$\approx\frac{\rho_o C_D}{2}\left[\left\sqrt{\left(\overline{u_{TE}}\right)^2+\left(\overline{v_{TE}}\right)^2}\right\left(\overline{u_{TE}}\right)+\left\sqrt{\left(\overline{u_P}\right)^2+\left(\overline{v_P}\right)^2}\right\left(\overline{u_P}\right)\right]$	$C_D = 0.005\ \rho_o C_D/2 = 2.6$ $C_D = 0.010\ \rho_o C_D/2 = 5.1$
$\underline{\text{BotStress}_y}$	$\left(\frac{1}{A}\left\langle\tau_y^b\right\rangle\right)$	$\approx\frac{\rho_o C_D}{2}\left[\left\sqrt{\left(\overline{u_{TE}}\right)^2+\left(\overline{v_{TE}}\right)^2}\right\left(\overline{v_{TE}}\right)+\left\sqrt{\left(\overline{u_P}\right)^2+\left(\overline{v_P}\right)^2}\right\left(\overline{v_P}\right)\right]$	$C_D = 0.005\ \rho_o C_D/2 = 2.6$ $C_D = 0.010\ \rho_o C_D/2 = 5.1$
$\underline{\text{LatStress}_x}$	$-\frac{1}{A}\left\langle\delta_y hT_x\right\rangle_x$	$\approx -L_D(=1)\left[\frac{\rho_o\overline{u_D}\,\overline{u_D}}{\Delta y h_D}+\frac{\rho_o\overline{u_P}\,\overline{u_P}}{\Delta y h_P}\right]$	$\frac{\rho_o}{\Delta y h_D} = 7.45x10^{-3}\frac{kg}{m^5}$ $\frac{\rho_o}{\Delta y h_P} = 8.2x10^{-3}\frac{kg}{m^5}$
$\underline{\text{LatStress}_y}$	$-\frac{1}{A}\left\langle\delta_x hT_y\right\rangle_y$	$\approx -L_D(=1)\left[\frac{\rho_o\overline{v_P}\,\overline{v_P}}{\Delta x h_P}+\frac{\rho_o\overline{v_{TE}}\,\overline{v_{TE}}}{\Delta x h_{TE}}\right]$	$\frac{\rho_o}{\Delta x h_P} = 2.21x10^{-3}\frac{kg}{m^5}$ $\frac{\rho_o}{\Delta x h_{TE}} = 5.10x10^{-3}\frac{kg}{m^5}$

Table B3c OBSERVED *Outer Zone* ESTIMATES: A summary of the approximations and corresponding assumptions used to estimate the *rotated velocity-related terms* (units Pa = N/m^2) in the volume-integrated momentum equations according to Eq (B2); using *observed* hindcast series; with subscripts referenced to stations IDs in Figure 9; and Δx = 15.47 km; Δy = 4.17 km; h_P= 30m; h_D = 33m; and h_A= 33m.

Data	Term	Estimate Algorithm	Constants
Outer	$[u]$	$\left\{\left(\overline{u_D}\right)0.5+0.5\overline{u_A}\right\}(\Delta x\Delta y)$	linear velocity variation
	$[v]$	$\left\{\left(\overline{v_D}\right)0.5+0.5\overline{v_A}\right\}(\Delta x\Delta y)$	linear velocity variation
Inertial_x	$\frac{\rho_o}{A}\frac{\delta[u]}{\delta t}$	$1025.7\frac{\delta}{\delta t}\left\{\left(\overline{u_D}\right)0.5+0.5\overline{u_A}\right\}$	$\rho_o = 1025.7 kg/m^3$
Inertial_y	$\frac{\rho_o}{A}\frac{\delta[v]}{\delta t}$	$1025.7\frac{\delta}{\delta t}\left\{\left(\overline{v_D}\right)0.5+0.5\overline{v_A}\right\}$	$\rho_o = 1025.7 kg/m^3$
Coriolis_x	$-\frac{\rho_o f}{A}[v]$	$-0.09905\left\{\left(\overline{v_D}\right)0.5+0.5\overline{v_A}\right\}$	$\rho_o f = 0.099 kg/s\cdot m^3$
Coriolis_y	$+\frac{\rho_o f}{A}[u]$	$0.09905\left\{\left(\overline{u_D}\right)0.5+0.5\overline{u_A}\right\}$	$\rho_o f = 0.099 kg/s\cdot m^3$
NonLinA_x	$\frac{\rho_o}{A}\left\langle\delta_x\overline{uu}\right\rangle_y$	$\left[\frac{\rho_o\overline{u_A}\overline{u_A}}{\Delta x h_A}-\frac{\rho_o\overline{u_D}\overline{u_D}}{\Delta x h_D}\right]$	$\frac{\rho_o}{\Delta x h_A}=2.01x10^{-3}\frac{kg}{m^5}$ $\frac{\rho_o}{\Delta x h_D}=2.01x10^{-3}\frac{kg}{m^5}$
NonLinB_x	$\frac{\rho_o}{A}\left\langle\delta_y\overline{uv}\right\rangle_x$	$\left[\frac{\rho_o\overline{u_D}\overline{v_D}}{\Delta y h_D}-\frac{\rho_o\overline{u_P}\overline{v_P}}{\Delta y h_P}\right]$	$\frac{\rho_o}{\Delta y h_D}=7.45x10^{-3}\frac{kg}{m^5}$ $\frac{\rho_o}{\Delta y h_P}=8.20x10^{-3}\frac{kg}{m^5}$
NonLinA_y	$\frac{\rho_o}{A}\left\langle\delta_x\overline{uv}\right\rangle_y$	$\left[\frac{\rho_o\overline{u_A}\overline{v_A}}{\Delta x h_A}-\frac{\rho_o\overline{u_D}\overline{v_D}}{\Delta x h_D}\right]$	ditto $\left\langle\delta_x\overline{uu}\right\rangle_y$ above
NonLinB_y	$\frac{\rho_o}{A}\left\langle\delta_y\overline{vv}\right\rangle_x$	$\left[\frac{\rho_o\overline{v_D}\overline{v_D}}{\Delta y h_D}-\frac{\rho_o\overline{v_P}\overline{v_P}}{\Delta y h_P}\right]$	ditto $\left\langle\delta_y\overline{uv}\right\rangle_x$ above
$\underline{\text{BotStress}_x}$	$\left(\frac{1}{A}\left\langle\tau_x^b\right\rangle\right)$	$\approx\frac{\rho_o C_D}{2}\left[\left\sqrt{\left(\overline{u_A}\right)^2+\left(\overline{v_A}\right)^2}\right\left(\overline{u_A}\right)+\left\sqrt{\left(\overline{u_D}\right)^2+\left(\overline{v_D}\right)^2}\right\left(\overline{u_D}\right)\right]$	$C_D=0.005\ \rho_o C_D/2=2.6$ $C_D=0.010\ \rho_o C_D/2=5.1$
$\underline{\text{BotStress}_y}$	$\left(\frac{1}{A}\left\langle\tau_y^b\right\rangle\right)$	$\approx\frac{\rho_o C_D}{2}\left[\left\sqrt{\left(\overline{u_A}\right)^2+\left(\overline{v_A}\right)^2}\right\left(\overline{v_A}\right)+\left\sqrt{\left(\overline{u_D}\right)^2+\left(\overline{v_D}\right)^2}\right\left(\overline{v_D}\right)\right]$	$C_D=0.005\ \rho_o C_D/2=2.6$ $C_D=0.010\ \rho_o C_D/2=5.1$
$\underline{\text{LatStress}_x}$	$-\frac{1}{A}\left\langle\delta_y hT_x\right\rangle_x$	$\approx -L_D(=1)\left[\frac{\rho_o\overline{u_D}\overline{u_D}}{\Delta y h_D}+\frac{\rho_o\overline{u_P}\overline{u_P}}{\Delta y h_P}\right]$	$\frac{\rho_o}{\Delta y h_D}=7.45x10^{-3}\frac{kg}{m^5}$ $\frac{\rho_o}{\Delta y h_P}=8.20x10^{-3}\frac{kg}{m^5}$
$\underline{\text{LatStess}_y}$	$-\frac{1}{A}\left\langle\delta_x hT_y\right\rangle_y$	$\approx -L_D(=1)\left[\frac{\rho_o\overline{v_A}\overline{v_A}}{\Delta x h_A}+\frac{\rho_o\overline{v_D}\overline{v_D}}{\Delta x h_D}\right]$	$\frac{\rho_o}{\Delta x h_A}=2.01x10^{-3}\frac{kg}{m^5}$ $\frac{\rho_o}{\Delta x h_D}=2.01x10^{-3}\frac{kg}{m^5}$

APPENDIX C: Vorticity Budget Term Estimation

The terms in the depth-averaged vorticity conservation Eq(3) (Table 12) have been estimated using the 5-tidal constituent hindcast series and the algorithms defined in Tables C1 and C2 for both the *Inner* and *Outer Zones* respectively.

Table C1 The *Inner Zone* algorithms used to estimate the terms in the relative vorticity conservation equation with hindcast 5-constituent tidal time series; assuming the total water depth H = a constant 23m. Here $\overline{\ldots}$ indicates vertical average. The drag coefficients C_D are multiplied by (0.36) to compensate for using depth averaged currents in the estimates (see main text). Subscripts refer to the stations in main text Figure 9. Constants are such that the term units are s^{-2}. δx = 15.47km; δy = 4.17km; H_I= 23m;

Term	Estimate Algorithm
$\frac{\partial \omega}{\partial t}$ local time rate change	$= \frac{\delta \omega_I}{\delta t}; where\ \omega_I = \left\{ \left[\frac{\delta\left(\overline{v_P} - \overline{v_{TTE}}\right)}{\delta x} \right] - \left[\frac{\delta\left(\overline{u_D} - \overline{u_P}\right)}{\delta y} \right] \right\}$
$u\frac{\partial \omega}{\partial x} + v\frac{\partial \omega}{\partial y}$ advection	$= \overline{u_I}\frac{\delta \omega_I}{\delta x} + \overline{v_I} O(0);$ where $\overline{u_I} = 0.5\left\{\overline{u_P} + \overline{u_{TTE}}\right\}, \overline{v_I} = 0.5\left\{\overline{v_P} + \overline{v_{TTE}}\right\}$; and $\frac{\delta \omega_I}{\delta x} = \frac{(\omega_O - \omega_I)}{\delta x}$
$A = \frac{\omega + f}{H}\left[\frac{\partial \eta}{\partial t} + \vec{u}\cdot\nabla H\right]$ stretching	$= \frac{\omega_I + f}{H_I}\left[\frac{\delta BP_{TTE}}{\rho g\, \delta t} + \left(\overline{u_I}\right)\frac{\delta H}{\delta x}\bigg|_I + \left(\overline{v_I}\right)\frac{\delta H}{\delta y}\bigg|_I \right];$ where $\frac{\delta H}{\delta x}\bigg|_I = 0.00119; \frac{\delta H}{\delta y}\bigg|_I = 0.00165$; H_I=23m
$I = -\frac{C_D \lvert \vec{u} \rvert}{H^2}\left[\vec{u}\times\nabla H\right]\cdot\vec{k}$ slope torque	$= -\frac{C_D SPD_I}{H_I^2}\left[\left(\overline{u_I}\right)\frac{\delta H}{\delta y}\bigg|_I - \left(\overline{v_I}\right)\frac{\delta H}{\delta x}\bigg|_I \right];$ where $SPD_I = \lvert \sqrt{\left(\overline{u_I}\right)^2 + \left(\overline{v_I}\right)^2} \rvert$
$II = \frac{C_D(\vec{u}\times\nabla \lvert \vec{u} \rvert)\cdot\vec{k}}{H}$ speed torque	$= \frac{C_D}{H_I}\left[u_I \frac{SPD_D - SPD_P}{\delta y} - v_I \frac{SPD_P - SPD_{TTE}}{\delta x} \right];$ where $SPD_D = \left(\sqrt{\left(\overline{u_D}\right)^2 + \left(\overline{v_D}\right)^2}\right); SPD_P = \left(\sqrt{\left(\overline{u_P}\right)^2 + \left(\overline{v_{PD}}\right)^2}\right);$ and $SPD_{TTE} = \left(\sqrt{\left(\overline{u_{TTE}}\right)^2 + \left(\overline{v_{TTE}}\right)^2}\right);$
$III = -\frac{C_D \lvert \vec{u} \rvert \omega}{H}$ dissipation	$= -\frac{C_D SPD_I}{H_I}\omega_I$
DRAG COEFFICIENTS	C_D=0.01; $\frac{C_D(0.6^2)}{H_I} = 0.000157$; $\frac{C_D(0.6^2)}{H_I^2} = 0.00000681$
$C = A_H \nabla^2 \omega$ diffusion	$= A_H \frac{\delta}{\delta x}\left(\frac{\delta \omega_I}{\delta x}\right)$ +O(0); where A_H=

Table C2 The *Outer Zone* algorithms used to estimate the terms in the relative vorticity conservation equation with hindcast 5-constituent tidal time series; assuming the total water depth H = a constant 33m. Here $\overline{\ldots\ldots}$ indicates vertical average. The drag coefficients C_D are multiplied by (0.36) to compensate for using depth-averaged instead of bottom currents in the estimates (see main text). Subscripts refer to the stations in main text Figure 9. Constants are such that the term units are s^{-2}.

Term	Estimate Algorithm
$\frac{\partial \omega}{\partial t}$ local time rate change	$= \frac{\delta \omega_O}{\delta t}; where\ \omega_O = \left\{ \left[\frac{\delta\left(\overline{v_A} - \overline{v_D}\right)}{\delta x} \right] - \left[\frac{\delta\left(\overline{u_D} - \overline{u_P}\right)}{\delta y} \right] \right\}$
$u\frac{\partial \omega}{\partial x} + v\frac{\partial \omega}{\partial y}$ advection	$= \overline{u_O}\frac{\delta \omega_O}{\delta x} + \overline{v_O} O(0);$ where $\overline{u_O} = 0.5\left\{\overline{u_A} + \overline{u_D}\right\}; \overline{v_O} = 0.5\left\{\overline{v_A} + \overline{v_D}\right\}$; and $\frac{\delta \omega_O}{\delta x} = \frac{(\omega_O - \omega_I)}{\delta x}$
$A = \frac{\omega + f}{H}\left[\frac{\partial \eta}{\partial t} + \vec{u} \cdot \nabla H\right]$ stretching	$= \frac{\omega_O + f}{H_O}\left[\frac{\delta BP_{TTE}}{\rho g \delta t} + \left(\overline{u_O}\right)\frac{\delta H}{\delta x}\bigg|_O + \left(\overline{v_O}\right)\frac{\delta H}{\delta y}\bigg|_O \right];$ where $\frac{\delta H}{\delta x}\bigg|_O = 0.00071; \frac{\delta H}{\delta y}\bigg|_I = 0.00297$; H_O=33m
$I = -\frac{C_D \lvert \vec{u} \rvert}{H^2}\left[\vec{u} \times \nabla H\right] \cdot \vec{k}$ slope torque	$= -\frac{C_D SPD_O}{{H_O}^2}\left[\left(\overline{u_O}\right)\frac{\delta H}{\delta y}\bigg|_O - \left(\overline{v_O}\right)\frac{\delta H}{\delta x}\bigg|_O \right];$ where $SPD_O = \lvert \sqrt{\left(\overline{u_O}\right)^2 + \left(\overline{v_O}\right)^2} \rvert$
$II = \frac{C_D(\vec{u} \times \nabla \lvert \vec{u} \rvert) \cdot \vec{k}}{H}$ speed torque	$= \frac{C_D}{H_O}\left[u_O \frac{SPD_D - SPD_P}{\delta y} - v_O \frac{SPD_A - SPD_D}{\delta x} \right];$ where $SPD_D = \left(\sqrt{\left(\overline{u_D}\right)^2 + \left(\overline{v_D}\right)^2} \right); SPD_P = \left(\sqrt{\left(\overline{u_P}\right)^2 + \left(\overline{v_{PD}}\right)^2} \right);$ and $SPD_A = \left(\sqrt{\left(\overline{u_A}\right)^2 + \left(\overline{v_A}\right)^2} \right);$
$III = -\frac{C_D \lvert \vec{u} \rvert \omega}{H}$ dissipation	$= -\frac{C_D SPD_O}{H_O}\omega_O$
DRAG COEFFICIENTS	C_D=0.01; $\frac{C_D(0.6^2)}{H_O} = 0.000109$ $\frac{C_D(0.6^2)}{{H_O}^2} = 0.00000331$
$C = A_H \nabla^2 \omega$ diffusion	$= A_H \frac{\delta}{\delta x}\left(\frac{\delta \omega_O}{\delta x}\right)$ +O(0); where A_H=

7. Acknowledgements

We gratefully acknowledge the cooperation and support of the US National Park Service, who provides space and infrastructure support for the CODAR instrumentation at their Cape Cod National Seashore station at Eastham, MA - near Nauset, MA. This publication is the result in part of research sponsored by The MIT Sea Grant College Program, under NOAA Grant Number NA06OAR4170019, MIT SG Project Number 2007-R/RC-104. This research has also been supported in part through a subcontract to Rutgers University who is the prime funded under NOAA grant NA07NOS4730221.

8. References

Black, K.P., and S.L. Gay, 1987. Eddy formation in unsteady flows. *J. Geophys.Res*. 92, 9514-9522.

Brown, W.S. and J.D. Irish, 1993.The annual variation of water mass structure in the Gulf of Maine, *J. Mar. Res.,* 51, 53-107.

Brown, W.S., 1984. A Comparison of Georges Bank, Gulf of Maine and New England Shelf Tidal Dynamics, *J. Phys. Oceanogr.,* 14, 145-167.

Brown, W.S., and Z. Yu, 2006. CODAR measurement and model simulation of transient tidal eddies in the western Gulf of Maine. University of Massachusetts, Dartmouth - School for Marine Science and Technology Technical Report SMAST 06-0503, pp 42.
http://www.smast.umassd.edu/OCEANOL/reports/CODAR/tidal_eddies_final_rpt_24may06.pdf

Brown W.S., G. M. Marques, S. King, C. Jakubiak, D. Brown, E. Levine, and L. Goodman, 2009. Transient tidal eddy project data report: winter 2008-09, University of Massachusetts, Dartmouth - School for Marine Science and Technology SMAST Technical Report 09-0204. pp43.
http://www.smast.umassd.edu/OCEANOL/reports/TTE/WINTER_08-09_DataRPT_13may09.pdf

Brown, W.S., and G.M. Marques, 2010. Transient tidal eddy motion in the western Gulf of Maine: WINTER, University of Massachusetts, Dartmouth - School for Marine Science and Technology SMAST Technical Report 10-0301, pp 53. http://www.smast.umassd.edu/OCEANOL/reports.php

Daifuku, P.R., and R.C. Beardsley, 1983. The K_1 Tide on the continental shelf from Nova Scotia to Cape Hatteras, *J. Phys. Oceanogr.,* 13(1),3-17.

Garrett, C., and R.H. Loucks, 1976. Upwelling along the Yarmouth shore of Nova Scotia. *J. Fish. Res. Board Can.* 33, 116-117.

Geyer, W.R., and R. Signell, 1990. Measurements of tidal flow around a headland with a shipboard acoustic doppler current profiler, *J. Geophys. Res*., 95, 3189-3197.

Geyer, W.R., 1993. Three-dimensional flow around headlands, *J. Geophys. Res.,* 98, 955-966.

Hench, J.L., and R.A. Leuttich, 2003. Transient tidal circulation and momentum balance at a shallow inlet. *J. Physical Oceanography* 33, 913-932.

Holboke, Monica J., 1998. "Variability of the Maine Coastal Current under Spring Conditions", Ph.D. Dissertation -Thayer School of Engineering -Dartmouth College, pp 193.

Lynch, D., and C. Naimie, 1992. The M2 tide and its residual on the outer banks of the Gulf of Maine. *J. Physical Oceanography* 23, 2222-2253.

Lynch, D.R., J.T.C. Ip, C.E. Naimie, and F.E. Werner, 1996. Comprehensive coastal

circulation model with application to the Gulf of Maine. *Continental Shelf Research*, 16, 875-906.

Lynch, D. R., M. J. Holboke, and C.E. Naimie, 1997. The Maine coastal current: spring climatological circulation. *Continental Shelf Research*, 17, 605-634.

Marques, G.M., and W.S. Brown, 2009. Project: Transient Tidal Eddies Model Configuration and Sensitivity, SMAST Technical Report SMAST 09-0207, pp 24. http://www.smast.umassd.edu/OCEANOL/reports/TTE/model_simulation_report_04may_2009.pdf

Marques, G.M., and W.S. Brown, 2011. Tidal Eddy Motions in the Western Gulf of Maine, Part 2: Secondary Flow, Submitted to this issue of *Continental Shelf Res*.

Moody, J., B. Butman, R.C. Beardsley, W.S. Brown**,** W. Boicourt, P. Daifuku, J.D. Irish, D.A. Mayer, H.E. Mofjeld, B. Petrie, S. Ramp, D. Smith and W.R. Wright, 1984."Atlas of Tidal Elevation and Current Observations on the Northeast American Continental Shelf and Slope," *U.S. Geological Survey Bulletin No. 1611*, U.S. Government Printing Office, pp. 122.

Mukai, A., R. Westerink, J. Luettich, and D. Mark (2002). Eastcoast 2001, a tidal constituent database for western north Atlantic, Gulf of Mexico, and Caribbean sea. Technical report, Coastal and Hydraulics Laboratory, US Army Corps of Engineers. http://www.unc.edu/ims/ccats/tides/tides.htm

Pingree, R., and L. Maddock, 1980. The effects of bottom friction and Earth's rotation on an island's wake. *J. Mar. Biol. Assoc. U.K.,* 60, 499-508.

Pingree, R., 1978. The formation of the Shambles and other banks by tidal stirring of the seas. *J. Mar. Biol. Assoc. U.K*, 58, 211-226.

Shcherbina, A. and G. Gawarkiewicz (2008). A coastal current in winter: Autonomous underwater vehicle observations of the coastal current east of Cape Cod., *J. Geophys. Res*., 113 (C07030), 15.

Signell, R., and W.R. Geyer, 1991. Transient eddy formation around headlands, *J. Geophys. Res., 96, 2561-2575.*

Stokesbury, K., B. Harris, M. Marino II, J. Nogueria, 2004. Estimation of sea scallop abundance using video survey in off-shore U.S. waters. *Journal of Shellfish Res.,* 23, 33-40.

Wolanski, E., T. Asaeda, A. Tanaka, and E. Deleersnijder, 1996. Three-dimensional island wakes in the field, laboratory experiments and numerical models. *Continental Shelf Res*.,16, 1437-1452.